---

**Article:**
Wagg, D.j. and Pei, J.-S. (Submitted: 2020) Modeling a helical fluid inerter system with time-invariant mem-models. engrXiv. (Submitted)

https://doi.org/10.31224/osf.io/8ybv6

---

# Modeling a Helical Fluid Inerter System with Time-Invariant Mem-Models

David J. Wagg[1] | Jin-Song Pei[2]

[1]Department of Mechanical Engineering, Sheffield University, Sheffield, UK
[2]School of Civil Engineering and Environmental Science, University of Oklahoma, Oklahoma, USA

**Correspondence**
*Jin-Song Pei, School of Civil Engineering and Environmental Science, University of Oklahoma, Norman, OK 73019. USA Email: jspei@ou.edu

**Abstract**

In this paper, experimental data from tests of a helical fluid inerter are used to model the observed hysteretic behaviour. The novel idea is to test the feasibility of employing mem-models, which are time-invariant herein, to capture the observed phenomena by using physically meaningful state variables. Firstly we use a Masing model concept, identified with a multilayer feedforward neural network to capture the physical characteristics of the hysteresis functions. Following this, a more refined approach based on the concept of a multi-element model including a mem-inerter is developed. This is compared with previous definitions in the literature and shown to be a more general model. Through-out this paper, numerical simulations are used to demonstrate the type of dynamic responses anticipated using the proposed time-invariant mem-models. Corresponding experimental measurements are processed to demonstrate and validate the new mem-modeling concepts. The results show that it is possible to have a unified model constructed using both the damper and inerter from the mem-model family. This model captures many of the more subtle features of the underlying physics, not captured by other forms of existing model.

**KEYWORDS:**
hysteresis; inerter; mem-models; dual input-output pairs; higher-order element; Masing model; mem-inerter

## 1 | INTRODUCTION

The inerter is a novel dynamic device that has been the subject of substantial research interest in both academia and industry. In particular, systems with inerters have been developed to improve passive control of dynamic systems, such as automotive suspensions, and more recently applications in civil engineering structures. This paper describes the development of a series of hysteresis models for an inerter by using new concepts recently introduced from other disciplines. The results are compared to experimental results from a fluid inerter system based on a fluid filled cylinder that induces flow in a helical pipe system.

The term inerter was first introduced by Smith (1) using the force-current analogy between mechanical and electrical networks. In this context, the inerter is considered to represent the equivalent of the capacitor. As a result it has the property that the force generated is proportional to the relative acceleration between its end points (or nodes). The constant of proportionality for the inerter is called inertance and is measured in kilograms.

Of course, in mechanical engineering the flywheel concept had been used for many centuries previously, but typically without relative accelerations. However in earthquake engineering, particularly in Japan since the late 1990s, several researchers have used inertial components to enhance the effectiveness of damping devices – see summary by (2) and references therein. There

are several types of inerters: the rack and pinion inerter (1), the ball screw inerter (3), the fluid inerter (4, 5, 6, 7), and the electromagnetic inerter (8, 9). There are three main application areas, vehicle suspensions systems (3, 10, 11, 12, 13, 14, 15), train suspension systems (16, 17), and civil engineering systems (18, 2, 19, 20, 21). The optimal performance of inerter-based vibration isolation systems has been considered by several authors, see for example the discussions in 22, 23, 24, 25. In general inertance is assumed to be fixed, but some recent devices have investigated the idea of variable inertance (26, 8, 5). The modeling in this study elucidates the natural variations in inertance that can occur in this type of fluid inerter.

Fluid inerters have the advantage of minimal moving parts, with the inertia effect being generated by the motion of the fluid. This inertial effect has two main ways of being realized. It is either due to the fluid driving a mechanical flywheel, which is usually called the hydraulic inerter (4), or the mass of the fluid itself moving in a helical pipe, which is defined as the helical fluid inerter, or just the helical inerter (5). In this paper we will describe the behavior of a helical inerter using memristive models, otherwise known as mem-models.

The models developed in this study, are based on two strategies: The first is a simplified modeling approach with two options, linear and nonlinear modeling, where the nonlinear modeling is a novel approach built on the dual input-output pairs in (27) and the Masing model for hysteresis. The second is a more refined modeling approach by following the mem-inerter framework outlined in (28), where we offer analysis on model complexity, supplement the switching behavior as in other mem-models, and assess the non-negativity of the identified inertance coefficient, $\boldsymbol{B}$.

Philosophically, we first identify a data-based model: the Masing model based on the experimental data. Then we use that to inform potential physics-based models, such as the nonlinear and mem-inerter model. We know that the physics-based models are simplifications of the real physics, but they are nonetheless very useful in the design and application of inerter devices. Due to the fact that there are a large number of data sets from the same inerter, we classify the majority of the test responses into two groups using a meaningful physical feature based on the mem-modeling. For each group, we come up with one simplified nonlinear model and another refined nonlinear model.

The rest of this paper is structured as follows. An overview of mem-modeling including the basic concepts a suite of carefully designed numerical demonstrations named "idealized responses" will be given in Section 2. An overview of all experimental data sets, preprocessing, and the extraction of typical one-cycle loops of the steady-state responses are given in Section 3 (Details of the experimental setup are included in Appendix A). Simplified modeling approaches and results are presented in Section 4, while the more refined modeling approach and results are given in Section 5. We conclude our study in Section 6.

## 2 | CONCEPTS AND NUMERICAL DEMONSTRATIONS

### 2.1 | Definitions for Mem-Models

Mem-models are briefly introduced here, following the derivations of (29). The family of mem-models contains both dampers and springs, and more. A mathematical parallelism exists in the definitions for these mem-models. We will seek to take advantage of this whilst remaining mindful of the differences in physics (27). A narrative definition for a *general* mem-model is as follows:

$$\text{state equations:} \qquad \text{rate of change for states} = \text{function of states, input, time} \tag{1}$$

$$\text{input-output equation:} \qquad \text{output} = \text{function of states, input, time} \times \text{input} \tag{2}$$

When time is dropped from the right-hand side of both state and input-output equations, the definition is for a time-invariant mem-model. Table 1 reviews the definitions for a *general* mem-dashpot model, also called memristive system model and a *general* mem-spring model, also called memcapacitive system model, and forecasts a new definition proposed in this study for a *general* mem-inerter model. $\boldsymbol{D}$, $\boldsymbol{S}$ and $\boldsymbol{B}$ may by considered generalized damping, spring and inertance coefficient, respectively.

**TABLE 1** Definitions of mem-models for a flow-controlled setting

| mem-dashpot (29) | mem-spring (29) | mem-inerter (this study) |
|---|---|---|
| $\dot{\mathbf{y}}_d(t) = \mathbf{g}_d\left(\mathbf{y}_d(t), \dot{x}(t), t\right)$ (3) | $\dot{\mathbf{y}}_s(t) = \mathbf{g}_s\left(\mathbf{y}_s(t), x(t), t\right)$ (5) | $\dot{\mathbf{y}}_i(t) = \mathbf{g}_i\left(\mathbf{y}_i(t), \dot{x}(t), t\right)$ (7) |
| $r_d(t) = D\left(\mathbf{y}_d(t), \dot{x}(t), t\right)\dot{x}(t)$ (4) | $r_s(t) = S\left(\mathbf{y}_s(t), x(t), t\right)x(t)$ (6) | $p_i(t) = B\left(\mathbf{y}_i(t), \dot{x}(t), t\right)\dot{x}(t)$ (8) |

For mem-dashpot and mem-spring, the choice of the states can be the traditional choice of displacement and velocity. More importantly as discussed in (29, 30), the choice of the state variables can be unique to account for memory effects by including absement $a$ and generalized momentum $p$, which are defined as the time integral of displacement $x$, and the time integral of the restoring force $r$, respectively. Note that $r$ will be taken as either $r_d$, $r_s$, the inerter restoring force $r_i$ (to be introduced later), or a combined element restoring force depending on the specific context. The corresponding $p$ will be $p_d$, $p_s$, and $p_i$, respectively. We have the relationship that

$$a(t) = \int_{-\infty}^{t} x(\tau)d\tau, \quad p(t) = \int_{-\infty}^{t} r(\tau)d\tau \tag{9}$$

Here, we follow (31) by naming $p$ generalized momentum (g-momentum) rather than momentum as was done in (29, 27).

The most prominent property of the mem-models would be the so-called "zero-crossing" or "origin-crossing" property, which means the following: for mem-dashpots, we have $\dot{x}$ and $r_d$ becoming zero simultaneously. For mem-springs, we have $x$ and $r_s$ becoming zero simultaneously.

Mem-models are fundamentally nonlinear models (32, 33, 34). This is a new kind of nonlinear model given the following facts: First, "mem" stands for memory. In engineering mechanics applications, mem-models are for modeling memory effect, i.e., hysteresis. In addition to the nonlinear state-space representation as seen in Eqs. (3) to (6) and the use of $a$ and $p$ as state variables (when proper), discrete variables (also called "memory parameters") are introduced in 29, 27, 30 to capture history-/path-dependency.

The wider concept of mem-models form a model class that goes beyond mem-dashpots and mem-springs. The mem-inerter, to be introduced below, is such an example. All mem-models share the origin-crossing property among others, making them distinctive from other commonly seen nonlinear systems. Broadly speaking, mem-models have a strong connection with higher-order elements (HOEs), to be introduced below, which are a new way of constructing and thinking about constitutive modeling by exhausting possible higher-orders of both kinetic and kinematic quantities. This further distinguishes mem-models from other typical nonlinear models.

We also would like to highlight the adjective "relative" for displacement to pave the road for the introduction of the mem-inerter. In fact, all kinematic quantities involved here including absement, displacement, velocity (and later, acceleration) are *relative* quantities being the difference of the two nodes that define the element. Mem-dampers and mem-springs are generalized dampers and springs, respectively. Relative velocity and relative displacement are specified for dampers and springs, e.g., in (35).

## 2.2 | Inerter Models

There are three sub-models of inerters.

A linear inerter is defined as follows:

$$p_i = B\dot{x} \tag{10}$$

where $B$ stands for inertance, with the unit of mass. The origin-crossing behavior is trivial, meaning that $\dot{x}$ and $p$ become zero simultaneously. This definition is consistent with the other one in (36), where a linear relationship between $\ddot{x}$ and $r$ is used. As mentioned previously, it should be emphasized that $x$ is a relative motion.

A nonlinear inerter is defined as

$$\hat{p}_i = \hat{B}(\dot{x}) \tag{11}$$

where the origin-crossing behavior is assumed because it is physically meaningful. Notice that this definition differs from that in (36), where the linear relationship between $\ddot{x}$ and $r$ is generalized.

Reference 28 proposes the concept of a mem-inerter and contrasts it with definitions of a linear and nonlinear inerter. The physical motivation seems to fit well with this study. This mem-inerter, which is assumed to be a displacement-dependent inerter function, is defined as

$$p_i = B(x)\dot{x} \tag{12}$$

Or, equivalently, there is a one-to-one mapping as follows

$$\phi = H(x) \tag{13}$$

where the integrated generalized-momentum is denoted as:

$$\phi(t) = \int_{-\infty}^{t} p_i(\tau)d\tau \tag{14}$$

and the subscript $i$ can be dropped for a more general definition of $\phi$. The time derivative of $H(x)$ is $B(x)\dot{x}$ after applying the chain rule.

This definition for the mem-inerter in (28) is not as comprehensive as those for memristive and memcapacitive system models. A *general* mem-inerter model *may* be defined as in Table 1. Making the definition time-invariant and when the state variable is further chosen as $x$, the time integral of the input $\dot{x}$ alone, we *could* have a simple time-invariant mem-inerter model as follows:

$$p_i = B(x, \dot{x})\dot{x} \tag{15}$$

Equations (7), (8), and (15) are the results of extending the mathematical parallelism in mem-models. In this study, we will demonstrate that these equations are useful in modeling certain types of inerter, such as the helical inerter. However, as will be seen, the behaviour of a physcial inerter is complex, and it therefore unlikely that it could be modeled as a mem-inerter *alone*. It should also be noted that the signals recorded from an inerter test (discussed in detail in Section 3) could be interpreted using other nonlinear models. What we aim to show here is that the mem-model approach provides a useful framework for capturing some of the more subtle behaviours exhibited by these systems. To do this, we will first provide a set of numerical examples to demonstrate the modeling capability of Eq. (15) alone. Later, we will seek a possible application of Eq. (15) to the experimental data from the helical inerter.

## 2.3 | Idealized Responses

Now we consider the idealized responses from these mem-elements.

The relative displacement $x(t)$ will be imposed as the input. From acceleration to absement, all time histories are computed from

$$\ddot{x}(t) = -A\omega^2 \sin(\omega t) \tag{16}$$

$$\dot{x}(t) = A\omega \cos(\omega t) \tag{17}$$

$$x(t) = A \sin(\omega t) \tag{18}$$

$$a(t) = \frac{A}{\omega} - \frac{A}{\omega} \cos(\omega t) \tag{19}$$

where $A = 1$ and $\omega = 1$ in this study.

Let us now take a mem-dashpot, a mem-spring, and a mem-inerter. Subjecting each to the defined sinusoidal input, we obtain the results shown in Figs. 1, 2 and 3. The responses of a linear dashpot, a linear spring, and a linear inerter are described in the captions of Figs. 1 and 2 for learning purpose. These mem-dashpot, mem-spring and mem-inerter are defined using $D$, $S$, and

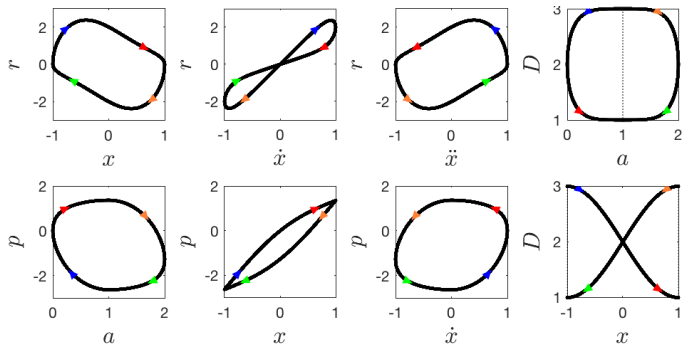


**FIGURE 1** A particular mem-dashpot subject to the prescribed sinusoidal displacement input. For a linear dashpot, from the left to right columns, there would be ellipses, straight lines with a positive slope, ellipses, and constants of the value of the slope for $D$

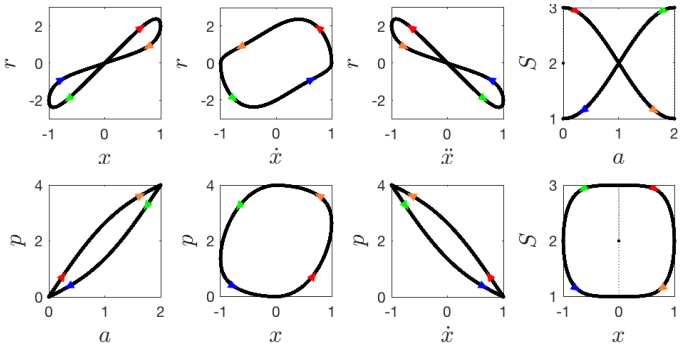


**FIGURE 2** A particular mem-spring subject to the prescribed sinusoidal displacement input. For a linear spring, from the left to right columns, there would be straight lines with a positive slope, ellipses, straight lines with the negative slope, and constants of the value of the positive slope for $S$. For a linear inerter, from the left to right columns, there would be straight lines with a negative slope, ellipses, straight lines with the positive slope, and constants of the value of the positive slope for $B$

$B$, respectively, as follows, each as a simple time-invariant system model:

mem-dashpot:
$$D = -\text{sgn}(\dot{x}) \sin\left(\frac{\pi}{2}x\right) + 2 \tag{20}$$

mem-spring:
$$S = \text{sgn}(x) \cos\left(\frac{\pi}{2}a\right) + 2 \tag{21}$$

mem-inerter:
$$B_1 = \frac{\text{sgn}(\dot{x}) + 1}{2} \frac{0.2}{1 + e^{-10x}} + \frac{\text{sgn}(\dot{x}) - 1}{2} \frac{-0.2}{1 + e^{10x}} \tag{22}$$

$$B_2 = \frac{\text{sgn}(\dot{x}) + 1}{2} \frac{0.2}{1 + e^{-10x-3}} + \frac{\text{sgn}(\dot{x}) - 1}{2} \frac{-0.2}{1 + e^{10x+3}} \tag{23}$$

$$B_3 = \frac{\text{sgn}(\dot{x}) + 1}{2} \frac{0.2}{1 + e^{-10x-3}} + \frac{\text{sgn}(\dot{x}) - 1}{2} \left(\frac{-0.2}{1 + e^{10x+3}} - 0.1\right) \tag{24}$$

Throughout this study, numerical differentiation with respect to time is carried out by using the central difference method. The MATLAB (37) code adopted here is central_diff.m (38) to ensure forward and backward differences at the left and right ends, respectively, and with the same second-order of accuracy as the central difference for the mid-portion. Numerical integration with respect to time is carried out by using the trapezoidal rule to obtain the integral counterpart for a specified input or solved output. Four colors, red, orange, green, and blue, highlight the responses to the four quarters of the sinusoidal input.

The origin-crossing property for the mem-dashpot, mem-spring and mem-inerter is prominent in the plots showing $r$ vs $\dot{x}$, $r$ vs $x$, and $p$ vs $\dot{x}$,respectively. The "figure of eight" structure of the response can be seen from the corresponding plots. Furthermore, the orientation of a loop can be observed following (29). For dashpots, $r$ vs $x$ rotates clockwise — it is symmetrical for a linear dashpot, while anti-symmetrical for a mem-dashpot. Similarly for springs, $r$ vs $\dot{x}$ rotates counter-clockwise, and likewise it is symmetrical for a linear spring, while anti-symmetrical for a mem-spring. Note also that the pairs of $p$ vs $x$, and $p$ vs $a$ rotate clockwise for the dashpots, while $p$ vs $x$ rotates counter-clockwise for the springs. For $p$ vs $a$, a mem-dashpot and mem-spring differ in terms of the shearing direction.

Column-wise in Fig. 3, three variations of a time-invariant mem-inerter model in the formulation of Eq. (15) are studied. While their different origin-crossing behaviors can be observed in the panels of $p$ vs $\dot{x}$ in the first row, the piecewise defined $B$ vs $x$ curves are plotted in last row with the equations given in Eqs. (22) to (24). Other rows in the middle reveal more inner-workings of the models. It can be seen that when $B_1$ vs $x$ switches between the two curves mirroring about $x = 0$, $p_1$ vs $\dot{x}$ is anti-symmetrical in the first and third quadrants. When the two curves on $B_2$ vs $x$ do not mirror about $x = 0$, $p_2$ vs $\dot{x}$ does not have the same loop in the first and third quadrants. When the two curves on $B_3$ vs $x$ become even more complex, $p_3$ vs $\dot{x}$ displays different loops in the first and third quadrants. This modeling capability of Eq. (15) will be used below to capture some of the subtle and complex physical behaviour observed in the experimental data from the helical inerter.

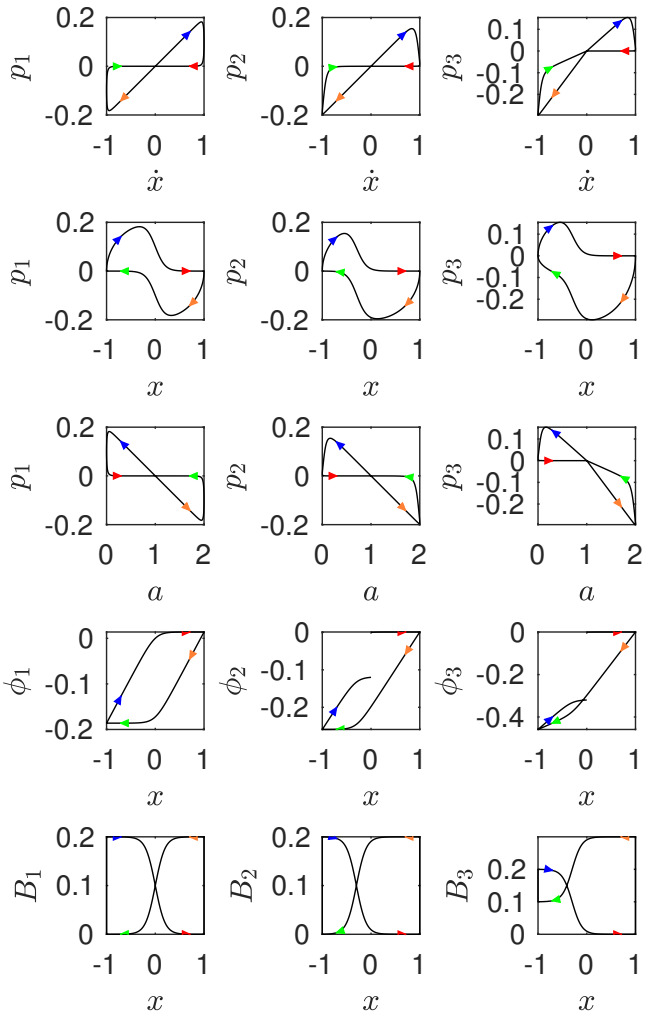


**FIGURE 3** Three particular mem-inerters (following subscripts 1, 2, and 3) with each subject to the prescribed sinusoidal displacement input

## 2.4 | Dual Input-Output Pairs, Masing Model, and Higher-Order Elements

Reference 27 bridges the gap between some commonly seen hysteresis models (e.g., Ramberg-Osgood (39), Bouc-Wen (40, 41), bilinear hysteresis (42, 43), and classical Preisach models (44, 45) and mem-models. The key idea in (27) is that the commonly seen hysteresis models are treated in the plane of $r$ vs $x$ where there are no origin-crossing properties due to permanent deformations involved, however all these models can be treated on the plane of $\dot{r}$ vs $\dot{x}$ instead, where there are origin-crossing properties given the piecewise-defined restoring forces. That is, both $\dot{x}$ and $\dot{r}$ become zero simultaneously. For these models, $r$ vs $x$ form an input-output pair called an integral pair, where $\dot{r}$ vs $\dot{x}$ form an input-output pair called a differential pair. Apart from the origin-crossing properties, these two pairs are inherently connected, for example, tangent quantities for an integral pair are secant quantities for a differential pair. Available models for integral pairs can be transformed to models for differential pairs.

In this study, we will investigate an alternative set of dual input-output pairs: the integral pair of $p$ vs $x$ and differential pair of $r$ vs $\dot{x}$. Initially, we will create a model for the inerter based on the pair of $p$ vs $x$, from which we will obtain the other quantities needed to define the pair of $r$ vs $\dot{x}$. The model for the $p$ vs $x$ is inspired by the Masing model that is typically used for modeling hysteretic behavior in the $r$ vs $x$ domain. See (46, 47, 48) for the Masing model for $r$ vs $x$ or equivalently, stress vs strain. This modeling approach is new, and we show that it is successful in using one model (i.e., the Masing model on $p$ vs $x$ plane) to capture some dominant features for multiple test data sets.

This initial success does not come as a surprise if we think broadly in terms of higher-order element (HOE) in multi-physics domain. Among other papers on this subject, (49) introduced the concept of ($\alpha$, $\beta$) elements, or higher-order elements for

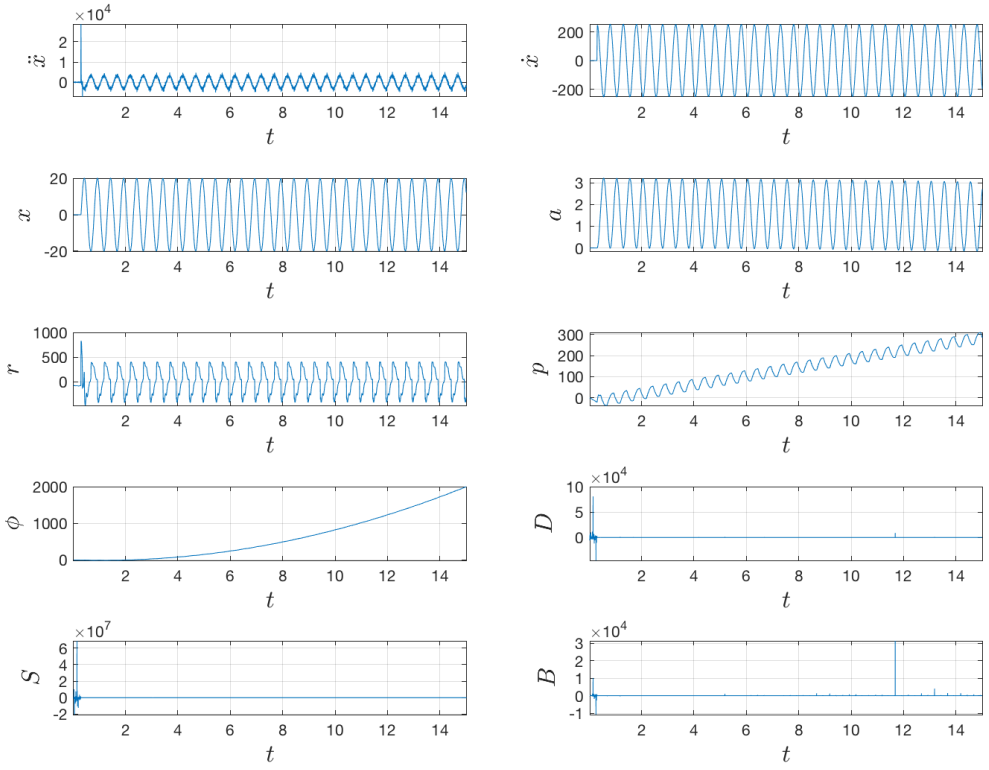


**FIGURE 4** Raw time histories of inerter response from the onset of a test: 20mm 2Hz

two-terminal electronic devices. Also, (50) further generalized the concept to other multiple physical domains. For mechanics, HOE promotes examining the derivatives and integrals of kinematic-kinetic pairs that we normally examine in order to define constitutive relations. Mem-models and inerters are just a special case of numerous HOEs.

## 3 | EXPERIMENTAL DATA

The experimental inerter test set-up has been previously described by (5), and for completeness a brief description is included in Appendix A. Using data from this set of experimental tests, a representative time history for the case where the inerter was subject to 2Hz sinusoidal excitation with a prescribed amplitude of 20mm is shown in Fig. 4. In this figure, only the displacement ($x$) and restoring force ($r$) time histories were recorded from the experiment. All the other time histories shown were obtained by post-processing the recorded results based on standard signal processing methods to obtain close approximations to the quantities defined in Section 2.

In Fig. 4, the integrated quantities, absement $a$, generalized-momentum $p$ and its integral $\phi$ can be seen to have drift and/or offset. This is primarily caused by numerical drift that is well known to occur in integrated quantities (51, 52). In order to mitigate these effects the MATLAB detrend function was applied to the recorded restoring force data to limit the effects on generalized momentum $p$ and its integral $\phi$. The resulting signals are shown in Fig. 5, where the restoring force $r$ has been detrended before any other numerical manipulation.

Figures 4 and 5 also show approximations to the quantities $D = \frac{r}{\dot{x}}$, $S = \frac{r}{x}$, and $B = \frac{p}{\dot{x}}$. It is important to clarify these computations are only meaningful for a mem-dashpot, mem-spring, and mem-inerter, respectively, and it is therefore to be expected that not all values in these time histories are physically meaningful, e.g., there are values of $D < 0$, $S < 0$, and $B < 0$. This supports the assertion that this type of inerter cannot be modeled as a single mem-element *alone*. The analysis of the recorded responses will enable us to develop a more sophisticated model which will be presented later in Section 5.

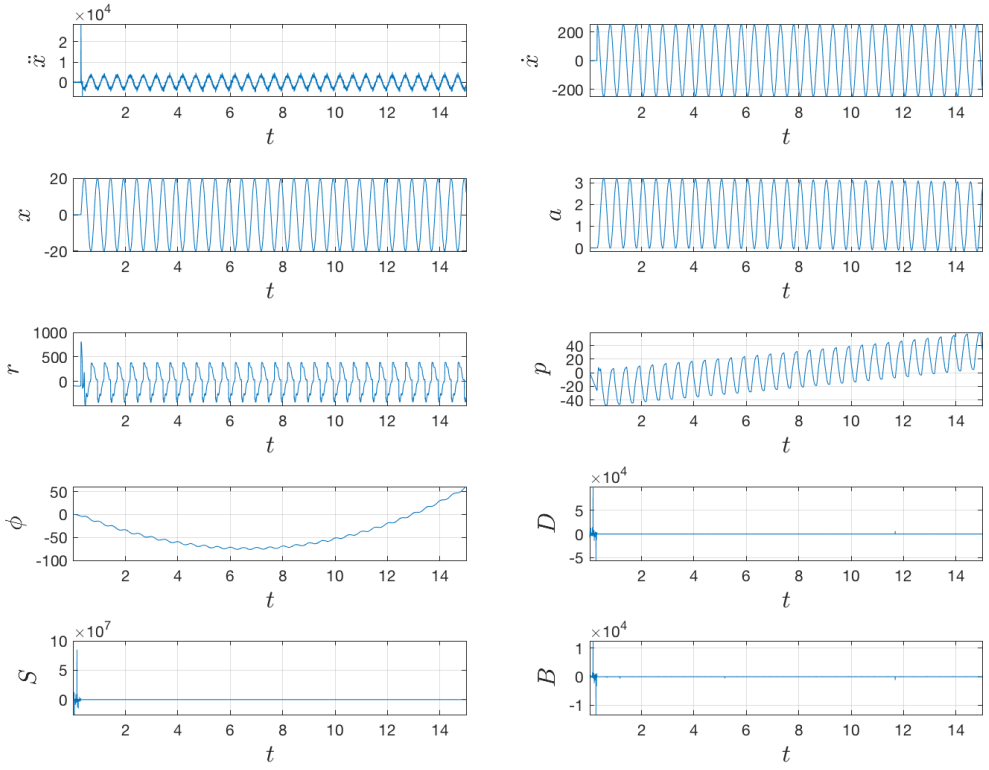


**FIGURE 5** Detrended time histories of inerter response from the onset of a test: 20mm 2Hz

In order to understand the physical behavior of the inerter system in more detail, the data from Fig. 5, was processed into a representative set of data for a single period of oscillation. The results are shown in Fig. 6. Here absement and generalized-momentum are numerically integrated from zero for each cycle.

In addition to time series representations, the data was plotted in the form of cyclic loops for a single steady-state oscillation, and the results are shown in Fig. 7. Four colored arrows, red, orange, green, and blue, again, highlight the responses to the four quarters of the sinusoidal input. The top row contains $r$ vs $\ddot{x}$, $r$ vs $\dot{x}$, $r$ vs $x$, and $\dot{x}$ vs $x$ plots, which are commonly used in analysis of cyclic signals. The bottom row contains $p$ vs $\dot{x}$, $p$ vs $x$, $p$ vs $a$, and $\phi$ vs $x$ plots, which will be examined closely in the rest of the paper following the concept of HOE. The key idea is that it may be challenging to create a model by using the commonly seen (top row) plots, however we may be able to seek insights and even solutions from those less commonly seen (bottom row) plots.

## 4 | SIMPLIFIED MODELING

In seeking to create an effective model of the inerter, we utilize the concept of higher-order elements (HOE) in conjunction with the Masing model. The initial step is to form two groups using the majority of the available test data sets. Group1 consists of the data sets which clearly exhibit memristive type behavior. Group 2 consists of the data sets that show a mixture of memristive and other behavior. Within each group, the analysis is the same. It is important to emphasize that this division criterion is arbitrary. However, it allowed us to carry out the subsequent analysis in a consistent manner.

Figures 8 and 9 contrast Groups 1 and 2 in terms of $r$ vs $\dot{x}$ origin-crossing behavior. Recalling the panel of $r$ vs $\dot{x}$ in Fig. 1, it can be seen that Group 1 display features of memristive system models given both the origin crossing and the switching behaviors from the unloading in the first quadrant (in red arrow) to the loading in the third quadrant (in orange arrow). Group 2, on the other hand, does not so clearly display the origin-crossing behavior (although some are close) and thus we assume that these would not be approximated well with memristive system models.

The next question is whether it is possible to approximate all test results within Group 1 using one model, and those within Group 2 using another model. This calls for an examination of the features of all test results within each group in a collective

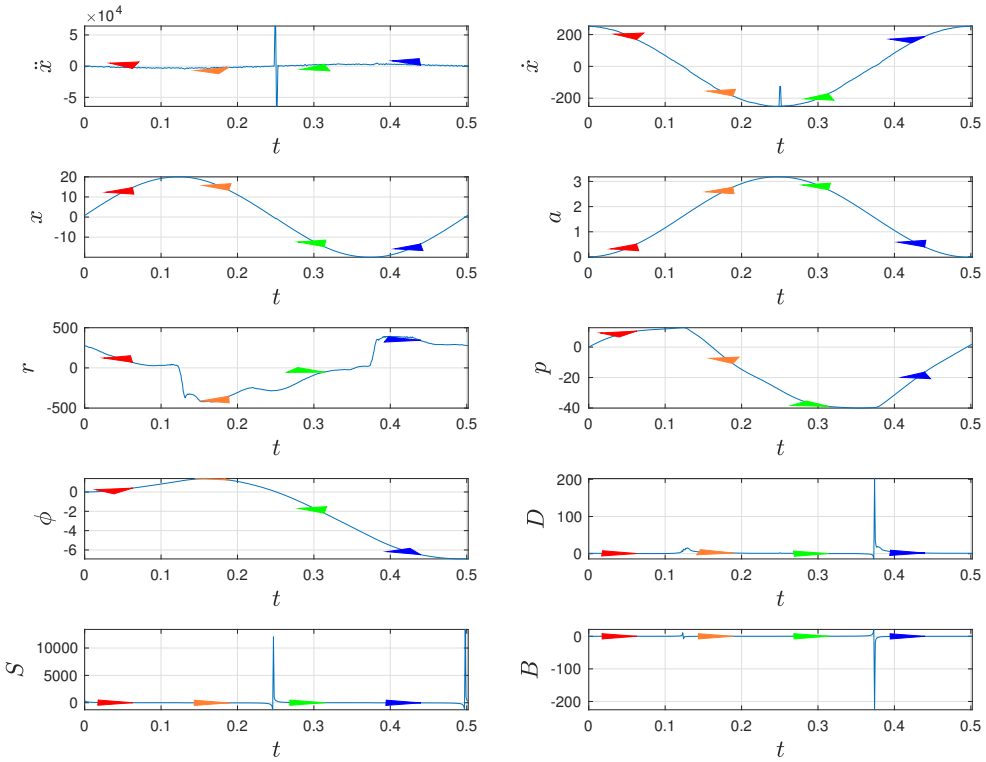


**FIGURE 6** Time histories of a typical one-cycle steady-state inerter response: 20mm 2Hz. Four colored arrows, red, orange, green, and blue, highlight the responses to the four quarters of the sinusoidal input

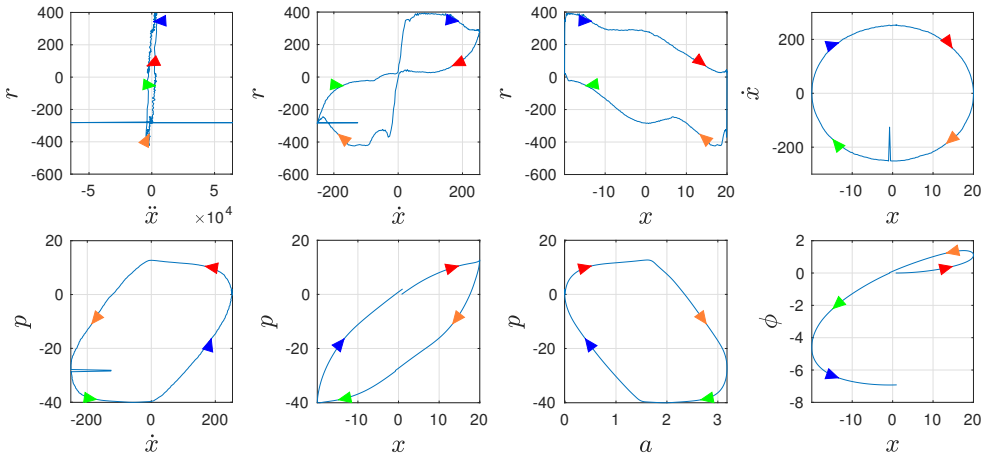


**FIGURE 7** Useful loops of a typical one-cycle steady-state inerter response: 20mm 2Hz

manner. To do so, we extract five consecutive loops from one test, and collect all test results within Group 1 that contains a total of 25 cycles. For Group 1, Fig. 10 helps examine possible underlying structure in terms of higher-order input-output pairs including $p$ vs $\dot{x}$, $p$ vs $x$, $p$ vs $a$, and $\phi$ vs $x$, respectively.

In order to make sense of these figures, we first focus on the $p$ vs $x$ plot in Fig. 10. Then we shift each loop in the $p$ vs $x$ so that they are all positioned with the same upper right vertex. This is the so-called shifted $p$ vs $x$ plot in Fig. 11. It indicates that all the data sets conform to one Masing model because each data set only corresponds to a different range of the same Masing model.

Note that the Masing model (46, 47, 48) has been used to model restoring force $r$ vs displacement $x$, or stress $\sigma$ vs strain $\varepsilon$ relations. Here we use the Masing model to model generalized momentum $p$ vs displacement $x$ relation instead. After the

**TABLE 2** Two groups of typical results selected from test data to demonstrate the usefulness of integral input-output pair using Masing model. Note that the data sets are labeled in terms of the input amplitude and frequency of the sinusoidal excitation

| Group 1: memristive system | Group 2: mixed behavior |
|---|---|
| 20mm 2Hz | 30mm 2Hz |
| 15mm 2Hz | 5mm 2Hz |
| 10mm 2Hz | 15mm 3Hz |
| 10mm 3Hz 3 | 2.5mm 7Hz |
| 5mm 4Hz | 2.5mm 10Hz |
| | 3mm 7Hz |
| | 2mm 10Hz |

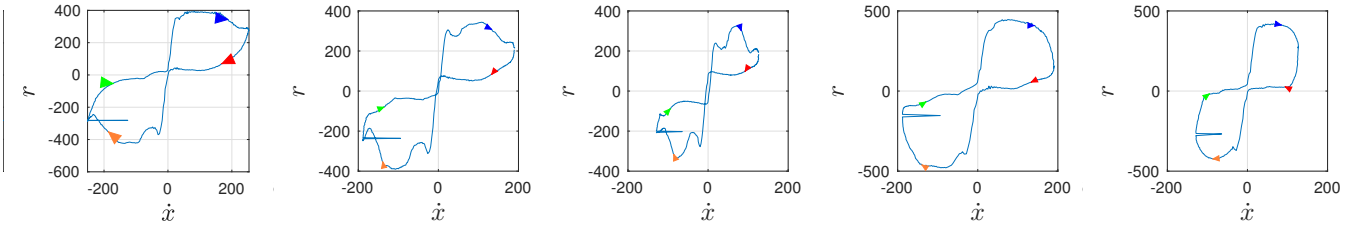


**FIGURE 8** Useful loops of a typical one-cycle steady-state inerter response showing the origin-crossing behavior on the $r$ vs $\dot{x}$ plane in an approximate sense: Group 1 in Table 2. From left to right, they are: 20mm 2Hz, 15mm 2Hz, 10mm 2Hz, 10mm 3Hz, and 5mm 4Hz

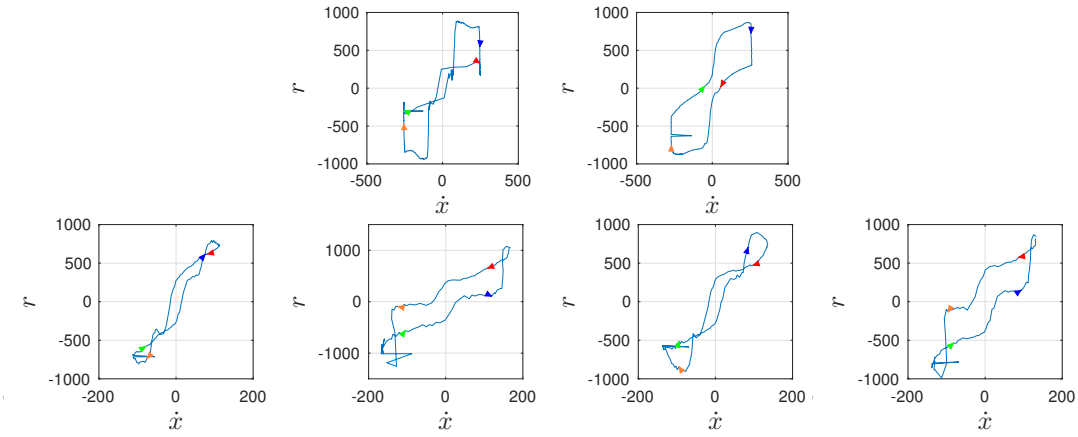


**FIGURE 9** Useful loops of a typical one-cycle steady-state inerter response *not* showing the origin-crossing on the $r$ vs $\dot{x}$ plane in an approximate sense: Group 2 in Table 2. From top to bottom and left to right, they are: 30mm 2Hz, 5mm 2Hz, 15mm 3Hz, 2.5mm 7Hz, 2.5mm 10Hz, 3mm 7Hz, and 2mm 10Hz

approximation, we will simply perform time derivatives on both generalized momentum $p$ and displacement $x$ to obtain a model for restoring force $r$ vs velocity $\dot{x}$, which is our true interest for characterizing the inerter behavior. This modeling strategy including leveraging and taking time derivatives follows the approach described in (27).

It should also be noticed that in the definition of the Masing model, as illustrated in Fig. 12, a virgin loading curve is critical because any other unloading and reloading curves are the scaled and shifted version of the virgin loading curve. However, in this specific application of the Masing model, we look into steady-state responses where we do not encounter the virgin loading curve anymore. Instead, we see only unloading and reloading curves.

In summary, $p$ vs $x$ pairs from the steady-state in different tests form different loops, the so-called hysteresis loops as in Fig. 10. These loops can be shifted and form a set in Fig. 11, which can be considered from the same Masing model in terms of

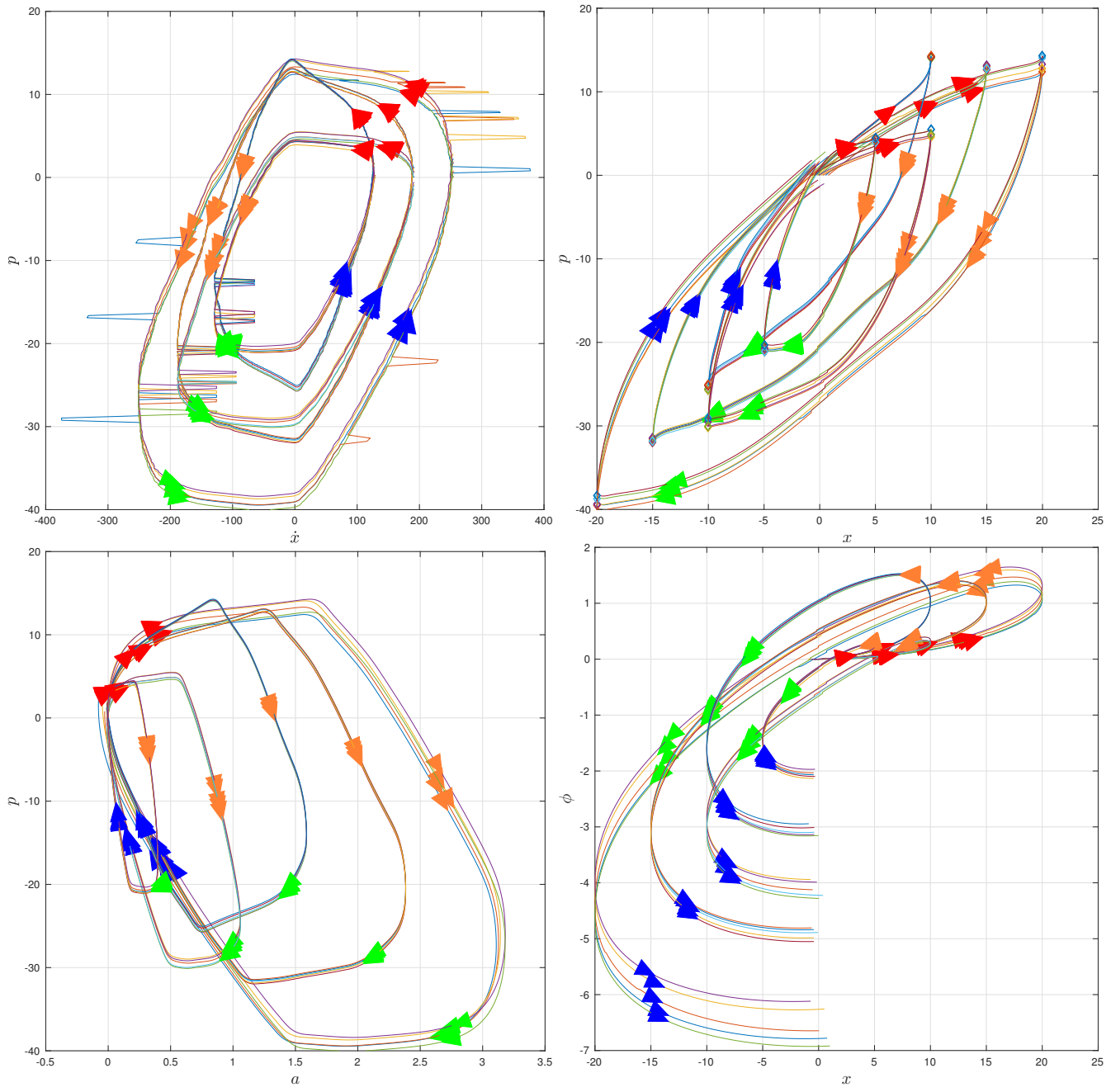


**FIGURE 10** $p$ vs $\dot{x}$, $p$ vs $x$, $p$ vs $a$, and $\phi$ vs $x$ plots of all data sets with a somewhat ambiguous underlying structure: Group 1 in Table 2

$p$ vs $x$ but with different turning points. Notice that shifting in an integral pair $p$ vs $x$ will not affect the differential pair $r$ vs $\dot{x}$ based on calculus.

Looking at Fig. 11, we decide to assume that all five tests are following the same unloading curve. Since the 20mm 2Hz test covers the largest range, we fit its unloading curve with a multilayer feedforward neural network (FFNN), a universal approximator. Five hidden nodes were chosen to produce the best approximation result. An alternative would be to collect the unloading curves of all tests for fitting, say, using an FFNN. Figure 13(a) presents the experimental unloading curve and trained unloading curve. In terms of the reloading curve, the Masing rule was used given the approximated unloading curve.

Figure 14 presents the time histories of the unloading curve followed by the reloading curve, which are consistent with Fig. 6 if we follow the colors in the order of orange, green, blue and red.

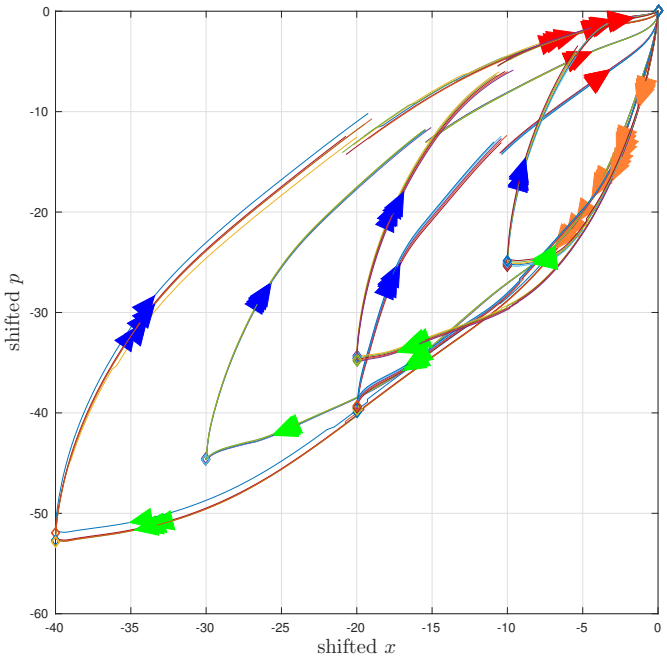


**FIGURE 11** $p$ vs $x$ plots with shifted $x$ and $p$ of all data sets indicating a clearer structure hinting an application of the Masing model: Group 1 in Table 2

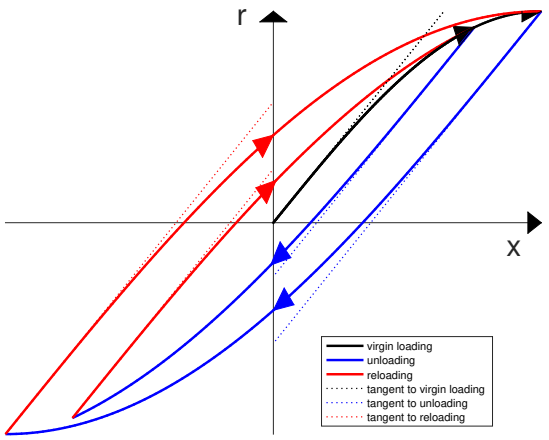


**FIGURE 12** A sketch of Masing model highlighting the identical initial slopes as in Fig. 11 and later utilized in Fig. 18

To predict the $r$ vs $\dot{x}$ plots for *all* other tests in Group 1, we will have to predict their corresponding $p$ vs $x$ plots first. As shown in Fig. 15, we used linear interpolation applied to a given time history $x$ with respect to that of 20mm 2Hz to obtain a portion of the 20mm 2Hz's time history $p$. This is not a perfect choice, as can be seen from Fig. 15, because not all time histories of $x$ fall 100% to the path of that for 20mm 2Hz, and so approximation errors are thus anticipated. We then numerically differentiate the given time history $x$ and predicted time history $p$ to obtained time histories of $\dot{x}$ and $r$, respectively, before combining them. Fig. 16 presents all predictions for the rest of the tests in Group 1.

The capability of the proposed modeling method has thus been demonstrated. Even though some of the more subtle behaviors are not entirely captured, the overall features and maximum $r$ values are represented to a reasonable degree using a unified model, especially when comparing with linear modeling where there isn't a unified model. Recall that we only need one data set for modeling, where the excitation frequency is relatively low (thus the range of $x$ is relatively high), to predict all of the rest of the responses given known displacement inputs. This is similar to some other techniques, when we intend to predict dynamic responses (with high frequencies) by using static or pseudo-static tests (with low frequencies).

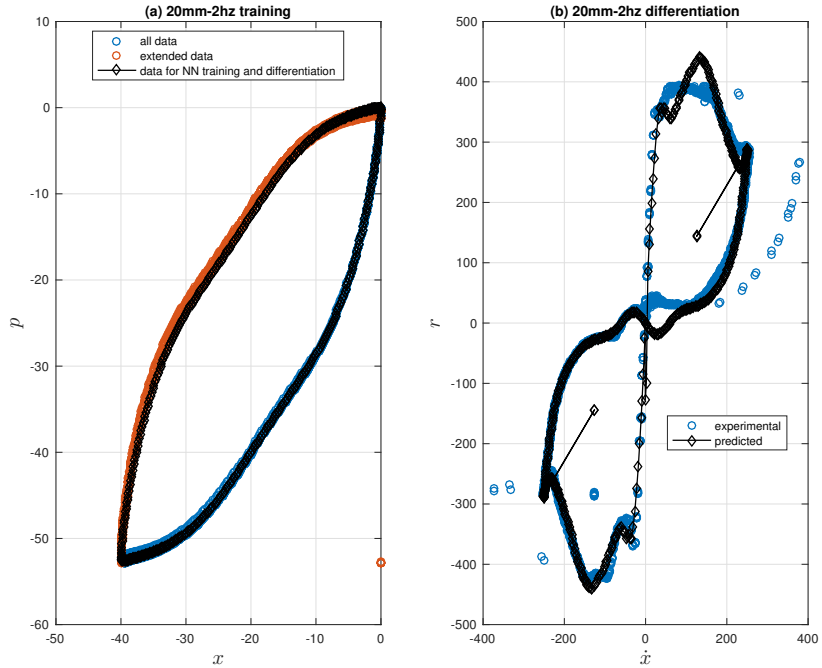


**FIGURE 13** The experimental and approximated dual input-output pairs for the 20mm 2Hz test in terms of (a) $p$ vs $x$, and (b) $r$ vs $\dot{x}$ plots. In detail, the FFNN was used to approximate the lower branch of $p$ vs $x$, while the upper branch was placed by following the Masing's rule. The $r$ vs $\dot{x}$ was simply obtained by differentiating the time histories of $p$ and $x$ before combining them

The same analysis and data processing are carried out to the Group 2 test results. See Figs. 17 to 22 for Group 2. The performance is not as good as that for Group 1, although there are some similar features.

It deserves serious thoughts on why the $p$ vs $x$ pair could be selected for fitting the Masing model by entirely following the experimental data. $p$ vs $x$ is an integral input-output pair for a mem-dashpot. A non-one-to-one but a looping $p$ vs $x$ as in a Masing model corresponds to a memristive system model as was studied in (27). This means that we chose the first approximation of the inerter by using a memristive system model (see both Eqs. (3) and (4) for the most comprehensive mathematical definition for a flow-controlled memristive system model). We do not claim that this modeling is completely accurate, however the feasibility should not come as a surprise. At least, both a helical fluid inerter and a mem-dashpot are variable energy-dissipative devices. Finally we observe that the mem-models fit best with input that are low frequency and large amplitude. This applies to most data sets in Group 1 and few in Group 2. This occurs because the time and amplitude range for the history-dependent effects to develop were more significant, and as a result we believe this is why the mem-modeling approach works better for this situation.

## 5 | MEM-INERTER MODELING

We now assume the inerter to be modeled is a parallel combination of mem-elements, dominated by the mem-inerter and a memristor. Initially we pose the problem by assuming that we are unsure of the exact type of elements in the model, and want to use the experimental data to identify this. We also investigate whether the definition for the mem-inerter in (28) is adequate in this context.

With these uncertainties regarding the sub-models in mind, we start with the following overall equations that are general and flexible enough to capture the points mentioned above. Thus we define our possible models as

$$p = \begin{cases} p_i + p_d = \underbrace{B(x)\dot{x}}_{\text{mem-inerter}} + \underbrace{G(x)}_{\text{memristor}}, \text{ or} & (25) \\ \hat{p}_i + p_d = \underbrace{\hat{p}(\dot{x})}_{\text{nonlinear inerter}} + \underbrace{G(x)}_{\text{memristor}} & (26) \end{cases}$$

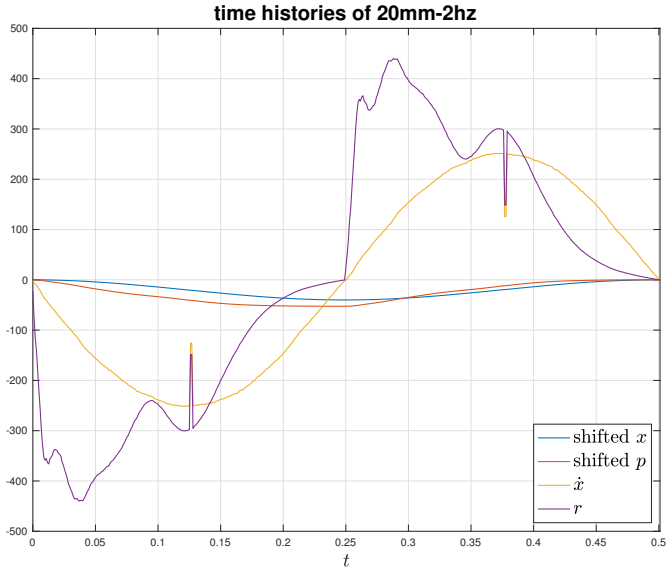


**FIGURE 14** The time histories used to plot the approximated results in Fig. 13, which compares favorably with Fig. 6 following the colors in the order of orange, green, blue and red

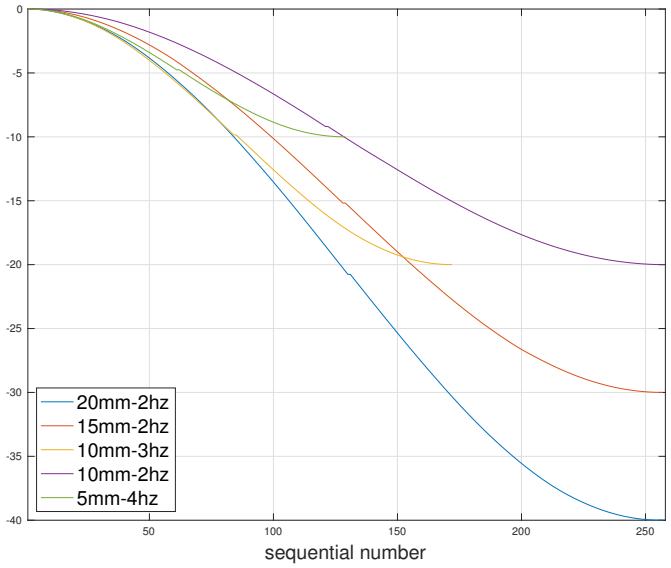


**FIGURE 15** The time history of $x$ belonging to the Group 1 tests revealing both the reason and error for linear interpolation

where the first terms on the righthand-side (RHS) account for the contribution from the inerter, while the second terms on RHS is from a damping element, assumed in the first instance to be a memristor. Capturing both variable inertance and variable damping follows well with the physics observed in the experiments. If the definition for the mem-inerter in Reference (28) is inadequate, then it would show up in the term of $B(x)$. We treat this as a model selection problem: Based on our identification, we choose the model that fits the data better.

First, when $\dot{x} = 0$ in either Eqs. (25) or (26), we can extract all points to model $p_d = G(x)$ for the memristor alone. If the identified function form is linear (without memory), then it means that there is only a linear dashpot. If the identified function is a one-to-one nonlinear function, then it means that there is a memristor. If the identified function is nonlinear but not one-to-one, it may indicate the need for a system-level model, a limitation discussed in Section 2.2. Two sets of these points are presented in Figs. 23 and 24 for Groups 1 and 2, respectively. An FFNN with three hidden nodes was used to fit each sets of the points; the

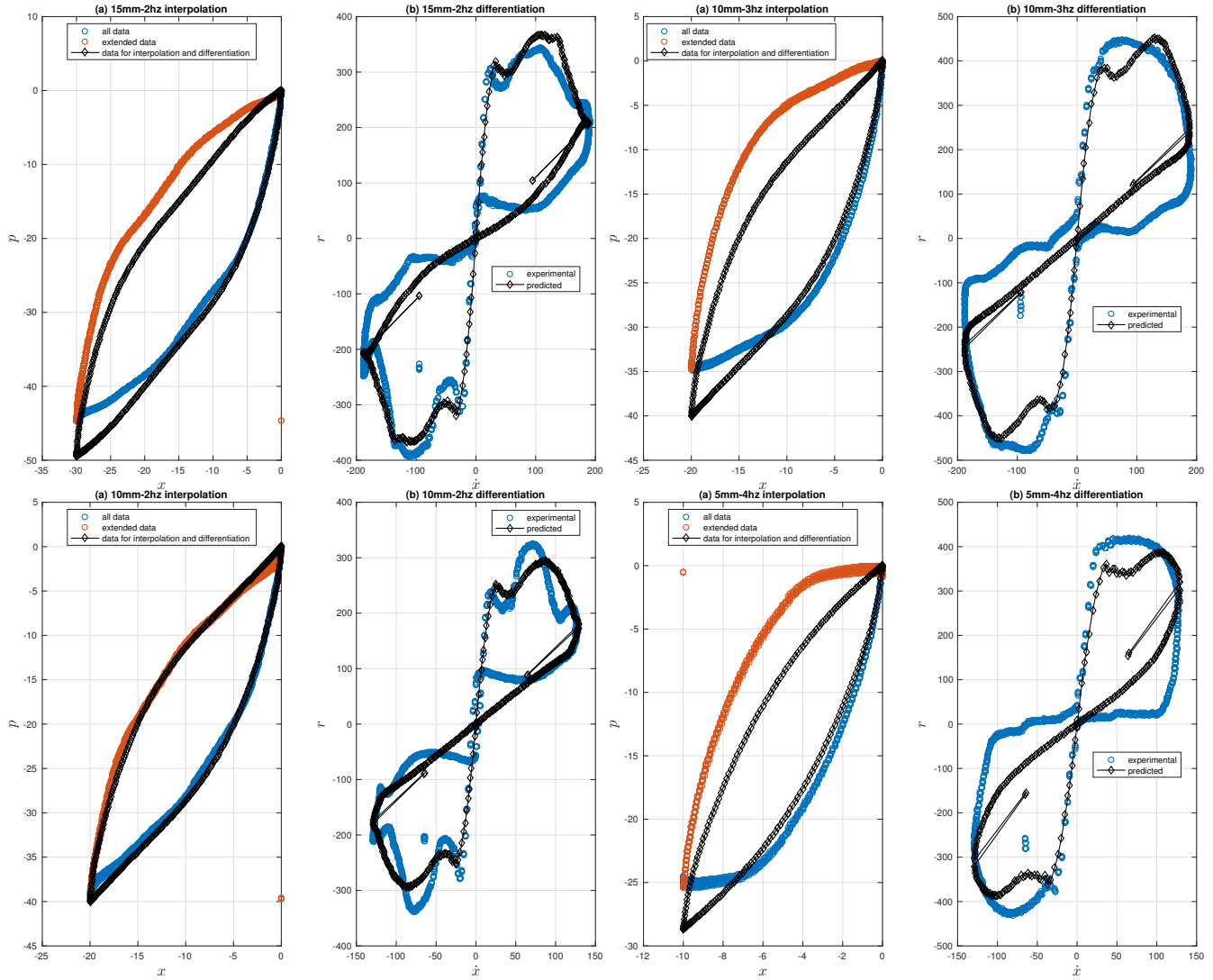


**FIGURE 16** The experimental and predicted dual input-output pairs for the 15mm 2Hz, 10mm 3Hz, 10mm 2Hz, and 5mm 4Hz test in terms of (a) $p$ vs $x$, and (b) $r$ vs $\dot{x}$ plots. In detail, the FFNN approximation and linear interpolation (see Fig. 15) were used to obtain the lower branch of $p$ vs $x$, while the upper branch was placed by following the Masing's rule. The $r$ vs $\dot{x}$ was simply obtained by differentiating the time histories of $p$ and $x$ before combining them

fitted results are presented in the same figures. We highlight that when $x = 0$, $p = 0$, and the first and third quadrant behaviors are not symmetrical.

To appreciate what the two fitted $p_d = G(x)$ curves mean, Figs. 25 and 26 present the $r$ vs $\dot{x}$ plots belonging to the memristor portions for all Groups 1 and 2 tests, respectively. Since the two fitted $p_d = G(x)$ functions are the integral pairs of the memristors, we used the experimental input $x$ as the domain of each $p_d = G(x)$, and obtained $p_d$ by simulating the trained FFNN. Then we numerically differentiated the time histories of both $x$ and $p_d$ before combining them for a $r_d$ vs $\dot{x}$ loop. The origin-crossing is anticipated for $r_d$ vs $\dot{x}$ with $r_d = D(x)\dot{x}$, where $D = \frac{dp_d}{dx}$. These loops do not have a switching feature because they are for memristors not memristive system models. There is a significant difference between Groups 1 and 2 in Figs. 25 and 26, respectively. It can also be seen that the consistency within Group 1 is better than that within Group 2.

The generalized momentum for the memristor portion, $p_d$, as just obtained was removed from the total generalized momentum to obtain the generalized momentum for the mem-inerter portion, $p_i$. Figs. 27 and 28 present all plots belonging to the mem-inerter portions for all Groups 1 and 2 tests, respectively. These plots include $\phi$ vs $x$, $p_i$ vs $\dot{x}$, and $B$ vs $x$, where both numerical differentiation and numerical integration were used, and $B = \frac{p_i}{\dot{x}}$.

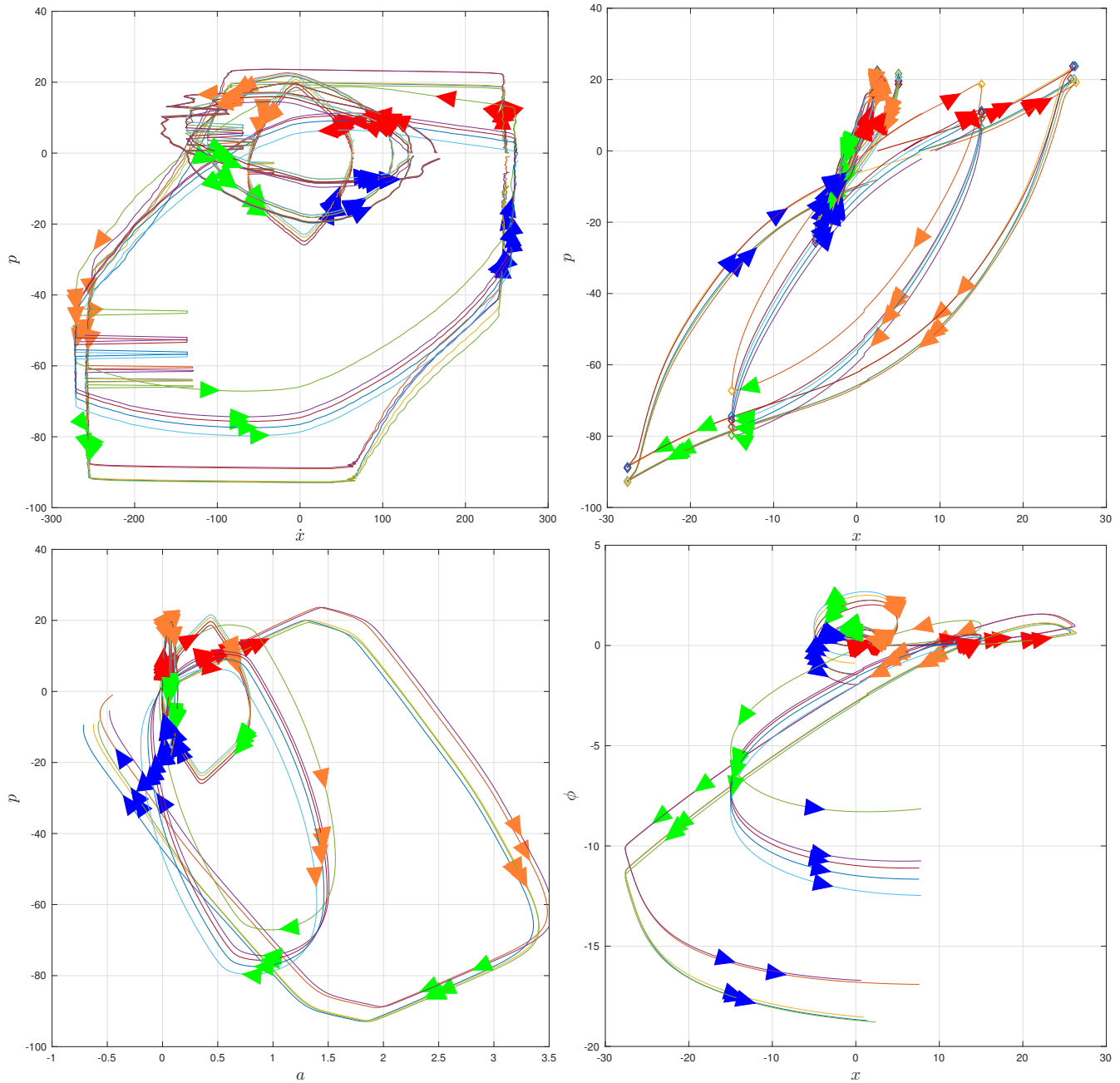


**FIGURE 17** $p$ vs $\dot{x}$, $p$ vs $x$, $p$ vs $a$, and $\phi$ vs $x$ plots of all data sets without a strong indication of underlying structure: Group 2 in Table 2

Four out of five $p_i$ vs $\dot{x}$ plots in Fig. 27 for Group 1 display the origin-crossing behavior, which is the signature of an inerter. Nonetheless, negative $B$ values on $B$ vs $x$ are not meaningful. It is not difficult to match $B < 0$ portion to those branches in the second and fourth quadrants on $p_i$ vs $\dot{x}$, very similar to disallowing $D < 0$ for the mem-dasphot in terms of $r_d$ vs $\dot{x}$. We can trim those physically meaningless portions.

Four out of five $B$ vs $x$ plots in Fig. 27 show some consistency, indicating the possibility of using *one* model for all tests in Group 1. It seems that there is *no* one-to-one mapping between $x$ and $B$. Instead, it seems that $B$ switches between two functions of $x$ according to $\dot{x}$. With this said, we can redefine the functional form of the model to be

$$p = p_i + p_d = \underbrace{B(x,\dot{x})\dot{x}}_{\text{mem-inerter}} + \underbrace{G(x)}_{\text{memristor}} \tag{27}$$

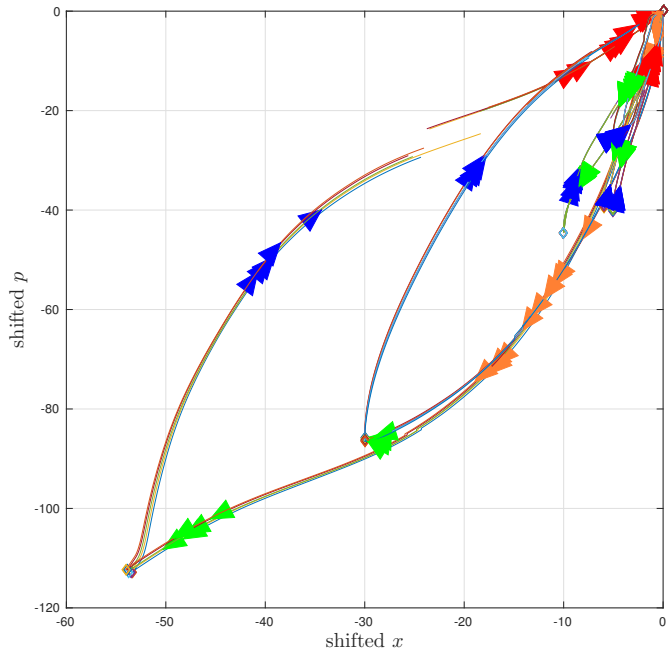


**FIGURE 18** $p$ vs $x$ plots with shifted $x$ and $p$ of all data sets indicating a clearer structure hinting an application of the Masing model: Group 2 in Table 2

meaning that indeed, the behaviour is better modelled by a mem-inerter, not a nonlinear inerter. In addition, this mem-inerter is more complicated than the definition in (28). This mem-inerter is a system-level model as proposed previously in Eq. (15). Similar to the system-level mem-models studied in (29), $\dot{x}$ switches between two functions of $B(x)$.

For Fig. 28 for Group 2, the majority of the plots do not carry physically meaningful $B$. The most meaningful test, is 30mm 2Hz which seems to be consistent with Eq. (27). From Table 2, Group 2 has more data sets with lower amplitude input and higher frequency, this will lead to lower amplitude outputs in general. We believe this indicates less opportunity for the fluid inerter system to develop time-integral-based memory effect, and as a result the mem-inerter is not such an effective model.

Now we can now qualitatively compare the five cases in both Figs. 27 and 28, (i.e., four out of Group 1 and one from Group 2) with those three numerical examples given previously in Fig. 3. In addition to finding similarities in terms of $p$ vs $\dot{x}$ and $B$ vs $x$, $\phi$ vs $x$ is now qualitatively comparable. In fact, these three numerical examples were inspired by the experimental results discussed here. As a result, we believe it is possible that Eqs. (22) to (24) could thus inspire more refined models using experimental data.

In terms of mem-inerter modeling, when $x = 0$ in either Eqs. (25) or (26) and when we also assume $G(0) = 0$, we can extract all points belonging to the inerter component meaning the $B$ and $\dot{x}$ terms, and the corresponding difference between the $p$ and $G$ terms. This is done but not presented here due to space considerations. It is uncertain how these points should be fitted making an origin-crossing curve. The differential pair is always more challenging to fit than its integral pair counterpart!

Finally, differentiating Eqs. (25) and (26), we have

$$r = \begin{cases} r_i + r_d = \underbrace{\dot{B}(x)\dot{x}^2 + B(x)\ddot{x}}_{\text{mem-inerter}} + \underbrace{D(x)\dot{x}}_{\text{memristor}}, \text{ or} & (28) \\ \hat{r}_i + r_d = \underbrace{\dot{\hat{p}}(\dot{x})\dot{x} + \hat{p}(\dot{x})\ddot{x}}_{\text{nonlinear inerter}} + \underbrace{D(x)\dot{x}}_{\text{memristor}} & (29) \end{cases}$$

When $\dot{x} = 0$, we can extract all corresponding $\ddot{x}$ so as to verify the existence of $B(x)$. If this does not go well for a specific set of data, it indicates that perhaps the inerter is a nonlinear inerter rather than a mem-inerter. Note that Eq. (28) differs from Eq. (11) in Reference (28) because the latter is differentiated from Eq. (12), a less general version than Eq. (25).

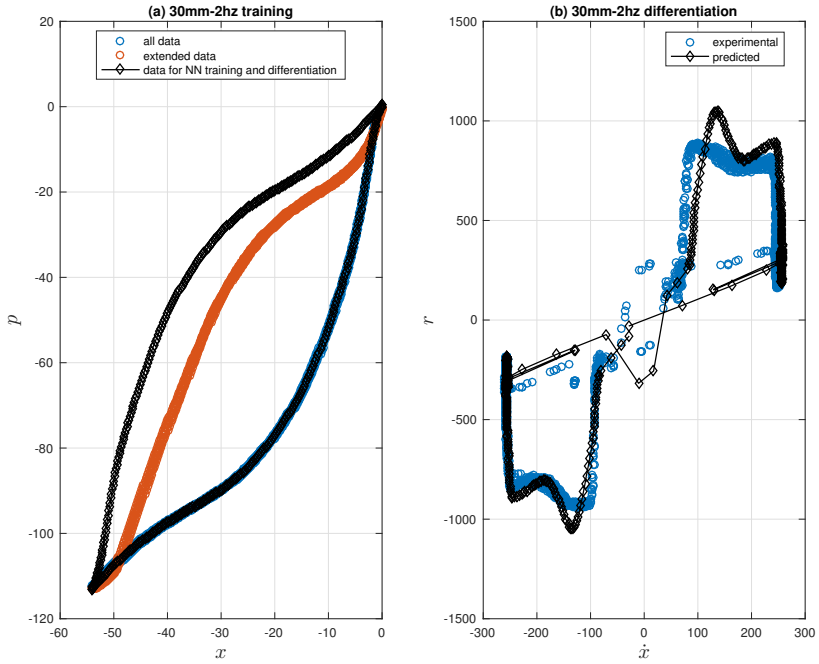


**FIGURE 19** The experimental and approximated dual input-output pairs for the 30mm 2Hz test in terms of (a) $p$ vs $x$, and (b) $r$ vs $\dot{x}$ plots. In detail, the FFNN was used to approximate the lower branch of $p$ vs $x$, while the upper branch was placed by following the Masing's rule. The $r$ vs $\dot{x}$ was simply obtained by differentiating the time histories of $p$ and $x$ before combining them

## 6 | CONCLUSION

The helical fluid inerter is a new device with important properties for passive structural control. Specifically it can provide both inertance and viscous damping simultaneously in a device with minimal moving components. However, its inherent hysteretic characteristics are quite challenging in terms of creating and effective model for the device. Our exploration in this study shows that some of the physics exhibited by the helical fluid inerter can be accurately captured using a newly developed theory called mem-models for hysteresis. More specifically, the functional relationships beyond the commonly-seen combinations among displacement, velocity, and restoring force have been demonstrated. These relationships depend on the integral quantities including absement, generalized momentum, and the integral of generalized momentum, which represent the natural memory effects that occur in the device.

By following the origin-crossing formulation of mem-modeling, which comes from the underlying instantaneous switching of the governing quantities, we have been able to demonstrate the effectiveness of the mem-modelling approach for the helical fluid inerter. In particular the results reported in this paper included both the Masing model (see Figs. 13 and 19 for training results and Figs. 16 and 22 for validation) and a more refined model (see both Fig. 3 and Eq. (27)).

We consider how a combination of mem-elements, such as mem-inerter and memristor may be used to capture more fully the physical behavior of the helical fluid inerter device. This also included a discussion of the subtle difference between the mem-inerter and a nonlinear inerter model – an important distinction when modelling practical devices. The results demonstrate that mem-modeling can enable engineers to build models of this type of device that more closely match the experimental data, and therefore give better validation results. Ultimately, we believe this will enable engineers to design helical fluid inerters with increased accuracy and therefore increased design confidence.

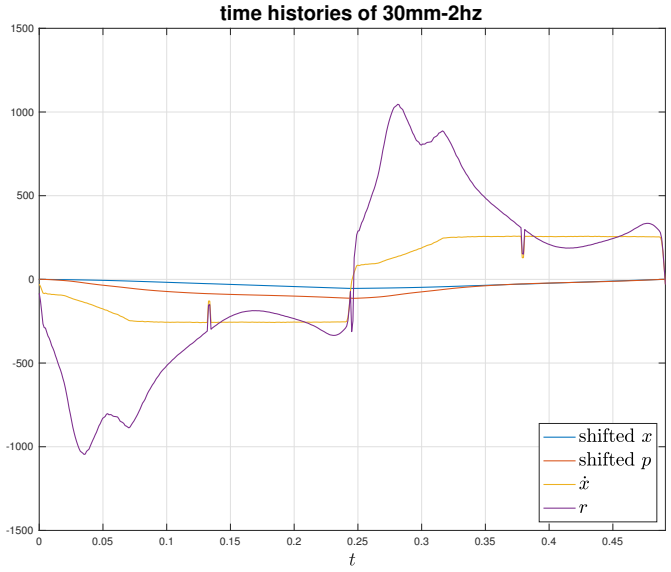


**FIGURE 20** The time histories used to plot the approximated results in Fig. 19, which compares favorably with the experimental time histories, which are not shown here

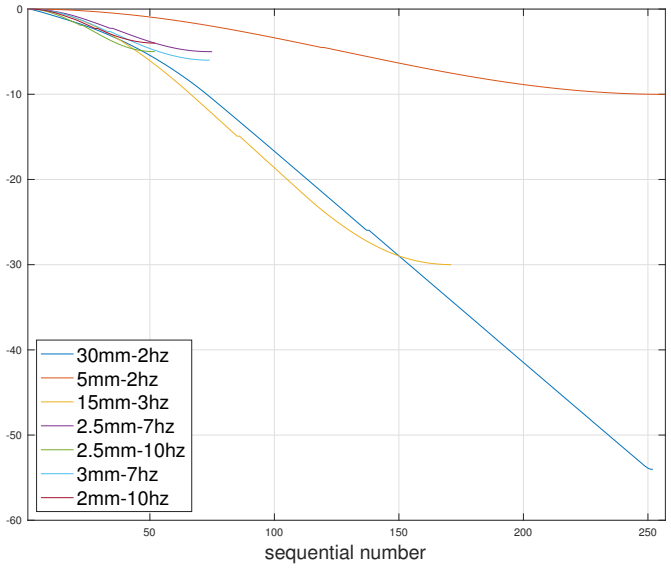


**FIGURE 21** The time history of $x$ belonging to the Group 2 tests revealing both the reason and error for linear interpolation

# APPENDIX

## A EXPERIMENTAL SETUP

Details of the experimental testing can be found in (5). For completeness a brief description of the system is included here. A schematic diagram of the fluid inerter system considered in this paper is shown in Fig. A1. The inerter system is designed with a central fluid filled cylinder, radius $r_2$, which is attached to a helical coil on the outside of the cylinder. The helical coil has an internal radius of $r_3$, and the helix radius is $r_4$. The fluid is driven through the cylinder using a plunger of radius $r_1$. Having a larger helix radius will lead to a higher inertance being generated by the fluid inerter system. In this paper the radius was set at its maximum possible value during testing of 120mm.

For the purpose of testing the inerter was installed in a test rig as shown in Fig. A2. The test rig consists of a hydraulic test

machine that can be used to give a dynamic displacement signal to the upper input of the inerter. The lower input of the inerter is constrained not to move, and connected to a force transducer. The upper input is attached to a hydraulic actuator, the position of which is measured with a linear variable differential transformer (LVDT). The actuator is controlled using bespoke computer software associated with the test machine. Finally, a laser thermometer was used to monitor the inerter temperature to ensure a consistent operating temperature. A close up photograph of the inerter system is shown in Fig. A2, where the helical pipe system can be clearly seen. The helical pipe was made of flexible tubing held in place by pipe clips. The central chamber was made of steel.

Details of the specific set-up parameters for each test phase are given in Table A1.

**TABLE A1** System parameters

| Property | Value | Units |
|---|---|---|
| Helix pitch, $h$ | 30 | mm |
| Wall thickness, $t$ | 5 | mm |
| $r_1$ | 14 | mm |
| $r_2$ | 25 | mm |
| $r_3$ | 6 | mm |
| $r_4$ | 120 | mm |
| Stroke of cylinder | 150 | mm |
| Kinematic viscosity at 40° | 2.1 | cSt |
| Oil density | 802 | kg/m$^3$ |

## B ACKNOWLEDGEMENTS

The Faculty Investment Program awarded by the Research Council at the University of Oklahoma is acknowledged for launching this collaboration. Professor Keith Worden is acknowledged for facilitating this collaboration. A discussion on the Masing model offered by Professor Jim Beck but not utilized in this study is appreciated.

## REFERENCES

1. Smith MC. Synthesis of Mechanical Networks: The Inerter. *IEEE Transactions on Automatic Control* 2002; 47: 1648-1662.

2. Ikago K, Kenji S, Norio I. Seismic control of single-degree-of-freedom structure using tuned viscous mass damper. *Earthquake Engineering & Structural Dynamics* 2012; 41(3): 453-474.

3. Chen MZQ, Papageorgiou C, Scheibe F, Wang FC, Smith MC. The missing mechanical circuit. *IEEE Circuits and Systems Magazine* 2009; 1531-636X: 10-26.

4. Wang FC, Hong MF, Lin TC. Designing and testing a hydraulic inerter. In: *Proceedings of the Institution of Mechanical Engineers, Part C: Journal of mechanical Engineering Science*. 225. ; 2010: 66-72.

5. Smith NDJ, Wagg DJ. A fluid inerter with variable inertance properties. In: *Proceedings of the 6th European Conference on Structural Control*; 2016; Sheffield: 1-8. Paper 192.

6. Liu X, Jiang JZ, Titurus B, Harrison A. Model identification methodology for fluid-based inerters. *Mechanical Systems and Signal Processing* 2018; 106: 479–494.

7. De Domenico D, Deastra P, Ricciardi G, Sims ND, Wagg DJ. Novel fluid inerter based tuned mass dampers for optimised structural control of base-isolated buildings. *Journal of the Franklin Institute* 2019; 356: 7626–7649.

8. Gonzalez-Buelga A, Clare LR, Neild SA, Jiang JZ, Inman DJ. An electromagnetic inerter-based vibration suppression device. *Smart Materials and Structures* 2015; 24(5): 055015.

9. Sugiura K, Watanabe Y, Asai T, Araki Y, Ikago K. Experimental characterization and performance improvement evaluation of an electromagnetic transducer utilizing a tuned inerter. *Journal of Vibration and Control* 2019: 1077546319876396.

10. Papageorgiou C, Smith MC. Laboratory experimental testing of inerters. In: *44th IEEE Conference on Decision and Control and the European Control Conference*; 2005; Seville, Spain: 3351-3356.

11. Papageorgiou C, Houghton NE, Smith MC. Experimental Testing and Analysis of Inerter Devices. *Journal of Dynamic Systems, Measurement and Control, ASME* 2009; 131: 011001-1 - 011001-11.

12. Shen Y, Chen L, Liu Y, Zhang X. Influence of fluid inerter nonlinearities on vehicle suspension performance. *Advances in Mechanical Engineering* 2017; 9(11): 1687814017737257.

13. Kuznetsov A, Mammadov M, Sultan I, Hajilarov E. Optimization of improved suspension system with inerter device of the quarter-car model in vibration analysis. *Arch. Applied Mechanics* 2011; 81: 1427-1437.

14. Wang FC, Chan HA. Vehicle suspensions with a mechatronic network strut.. *International Journal of Vehicle Mechanics and Mobility* 2011; 49(5): 811-830.

15. Evangelou S, Limebeer DJN, Sharp RS, Smith MC. Mechanical steering compensators for high-performance motorcycles. *Transactions of the ASME* 2007; 74: 332-346.

16. Wang FC, Liao MK, Liao BH, Su WJ, Chan HA. The performance improvements of train suspension systems with mechanical networks employing inerters. *International Journal of Vehicle Mechanics and Mobility* 2009; 47: 805-830.

17. Lewis T, Jiang J, Neild S, Gong C, Iwnicki S. Using an inerter-based suspension to improve both passenger comfort and track wear in railway vehicles. *Vehicle System Dynamics* 2019: 1–22.

18. Wang FC, Hong MF, Chen CW. Building suspensions with inerters. *Proceedings of the Institution of Mechanical Engineers, Part C: Journal of Mechanical Engineering Science* 2010; 224(8): 1605–1616.

19. Lazar IF, Neild SA, Wagg DJ. Using an inerter-based device for structural vibration suppression. *Earthquake Engineering & Structural Dynamics* 2014; 43(8): 1129-1147.

20. Giaralis A, Taflanidis AA. Reliability-based design of tuned mass-damper-inerter (tmdi) equipped multi-storey frame buildings under seismic excitation. In: *Proc. of 12th International Conference on Applications of Statistics and Probability in Civil Engineering, ICASP12*; 2015.

21. Lazar IF, Neild SA, Wagg DJ. Vibration suppression of cables using tuned inerter dampers. *Engineering Structures* 2016; 122: 62-71.

22. Scheibe F, Smith MC. Analytical solutions for optimal ride comfort and tyre grip for passive vehicle suspensions. *Journal of Vehicle System Dynamics* 2009; 47: 1229-1252.

23. Smith MC, Wang FC. Performance benefits in passive vehicle suspensions employing inerters. *Journal of Vehicle System Dynamics* 2004; 42: 235-257.

24. Wang FC, Su WJ. Impact of inerter nonlinearities on vehicle suspension control. *International Journal of Vehicle Mechanics and Mobility* 2008; 46: 575-595.

25. Krenk S, Høgsberg J. Tuned resonant mass or inerter-based absorbers: unified calibration with quasi-dynamic flexibility and inertia correction. *Proc. R. Soc. A* 2016; 472: 20150718.

26. Brzeski P, Kapitaniak T, Perlikowski P. Novel type of tuned mass damper with inerter which enables changes of inertance. *Journal of Sound and Vibration* 2015; 349: 56-66.

27. Pei JS, Gay-Balmaz F, Wright JP, Todd MD, Masri SF. Dual input-output pairs for modeling hysteresis inspired by mem-models. *Nonlinear Dynamics* 2017; 88(4): 2435-2455.

28. Zhang XL, Gao Q, Nie J. The mem-inerter: A new mechanical element with memory. *Advances in Mechanical Engineering* 2018; 10(6): 1-13.

29. Pei JS, Wright JP, Todd MD, Masri SF, Gay-Balmaz F. Understanding memristors and memcapacitors for engineering mechanical applications. *Nonlinear Dynamics* 2015; 80(1): 457-489.

30. Pei JS. Mem-spring models combined with hybrid dynamical system approach to represent material behavior. *ASCE Journal of Engineering Mechanics* 2018.

31. Pei JS, Wright JP, Gay-Balmaz F, Beck JL, Todd MD. On choosing state variables for piecewise-smooth dynamical system simulations. *Nonlinear Dynamics* 2018.

32. Chua LO. Memrister - The Missing Circuit Element. *IEEE Transactions on Circuit Theory* 1971; CT-18(5): 507-519.

33. Chua LO, Kang SM. Memristive Devices and Systems. In: *Proceedings of the IEEE*. 64. ; 1976: 209-223.

34. Di Ventra M, Pershin YV, Chua LO. Circuit Elements with Memory: Memristors, Memcapacitors, and Meminductors. In: *Proceedings of IEEE*. 97. ; 2009: 1717-1724.

35. Karnopp DC, Margolis DL, Rosenberg RC. *System Dynamics: Modeling, Simulation, and Control of Mechatronic Systems*. John Wiley & Sons, Inc. 5 ed. 2012.

36. Biolek D, Biolek Z, Biolkova V, Kokla Z. Nonlinear Inerter in the Light of Chua's Table of Higher-Order Electrical Elements. In: *2016 IEEE Asia Pacific Conference on Circuits and Systems (APCCAS)*; 2016; Jeju, South Korea: 617 - 620.

37. The Mathworks, Inc.*MATLAB*. 2010. http://www.mathworks.com/.

38. Canfield R. central_diff.m. http://www.mathworks.com/matlabcentral/fileexchange/12-central-diff-m/content/central_diff.m; 2015.

39. Jennings PC. Periodic Response of a General Yielding Structure. *Journal of the Engineering Mechanics Division, Proceedings of the American Society of Civil Engineers* 1964; 90(EM2): 131-166.

40. Bouc R. Modèle mathématique d'hystérésis. *Acustica* 1971; 21: 16-25.

41. Wen YK. Equivalent Linearization for Hysteretic Systems Under Random Excitation. *ASME Journal of Applied Mechanics* 1980; 47: 150-154.

42. Caughey TK. Sinusoidal Excitation of a System with Bilinear Hysteresis. *Journal of Applied Mechanics* 1960; 27: 640-643.

43. Caughey TK. Random Excitation of a System with Bilinear Hysteresis. *Journal of Applied Mechanics* 1960; 27: 649-652.

44. Krasnosel'skii MA, Pokrovskii AV. *Systems with Hysteresis*. Springer-Verlag . 1989.

45. Mayergoyz I. *Mathematical Models of Hysteresis*. Springer-Verlag . 1991.

46. Jayakumar P. *Modeling and Identification in Structural Dynamics*. PhD thesis. California Institute of Technology, Pasadena, CA; 1987.

47. Jayakumar P, Beck JL. System Identification Using Nonlinear Structural Models. In: Nake HG, Yao JTP., eds. *Structural Safety Evaluation Based on System Identification Approaches*. Proceedings of the Workshop at Lambrecht/Pfalz of *Vieweg International Scientific Book Series*. Friedr. Vieweg & Sohn Braunschweig/Wiesbaden; 1988: 82-102.

48. Beck JL, Jayakumar P. Class of Masing Models for Plastic Hysteresis in Structures. In: *Proceedings 14th ASCE Structures Congress*; 1996; Chicago, IL.

49. Chua L. Nonlinear circuit foundations for nanodevices. I. The four-element torus. In: *Proceedings of the IEEE*. 91. ; 2003.

50. Biolek D, Biolek Z, Biolkova V. Memristors and other higher-order elements in generalized through-across domain. In: *Proceedings of the 2016 IEEE International Conference on Electronics, Circuits and Systems (ICECS)*; 2016; Monte Caro, Monaco.

51. Worden K. Data Processing and Experiment Design for the Restoring Force Surface Method, Part I: Integration and Differentiation of Measured Time Data. *Mechanical Systems and Signal Processing* 1990; 4(4): 295-319.

52. Worden K. Data Processing and Experiment Design for the Restoring Force Surface Method, Part II: Choice of Excitation Signal. *Mechanical Systems and Signal Processing* 1990; 4(4): 321-344.

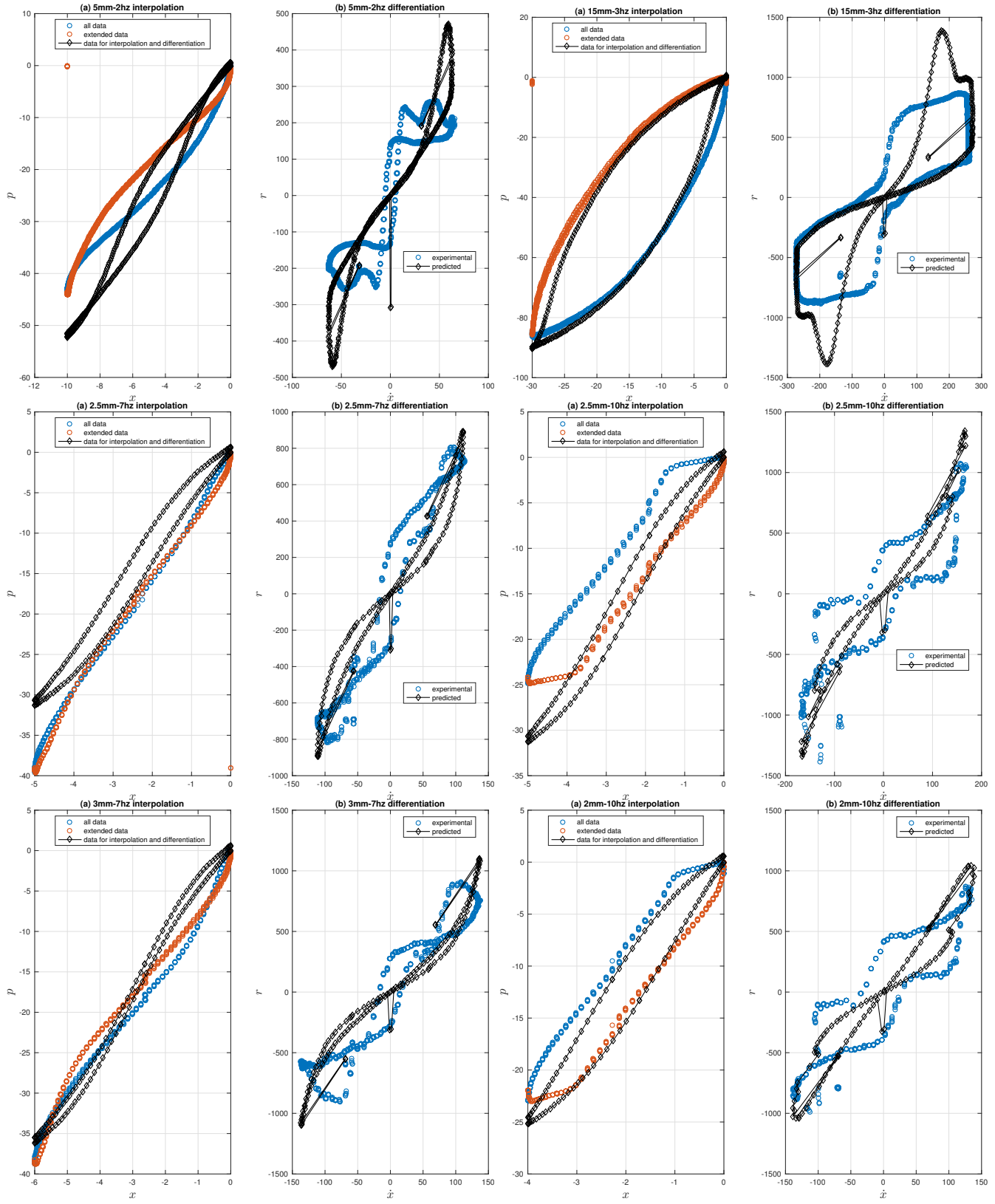


**FIGURE 22** The experimental and predicted dual input-output pairs for the 5mm 2Hz, 15mm 3Hz, 2.5mm 7Hz, 2.5mm 10Hz, 3mm 7Hz, and 2mm 10Hz test in terms of (a) $p$ vs $x$, and (b) $r$ vs $\dot{x}$ plots. In detail, the FFNN approximation and linear interpolation (see Fig. 21) were used to obtain the lower branch of $p$ vs $x$, while the upper branch was placed by following the Masing's rule. The $r$ vs $\dot{x}$ was simply obtained by differentiating the time histories of $p$ and $x$ before combining them

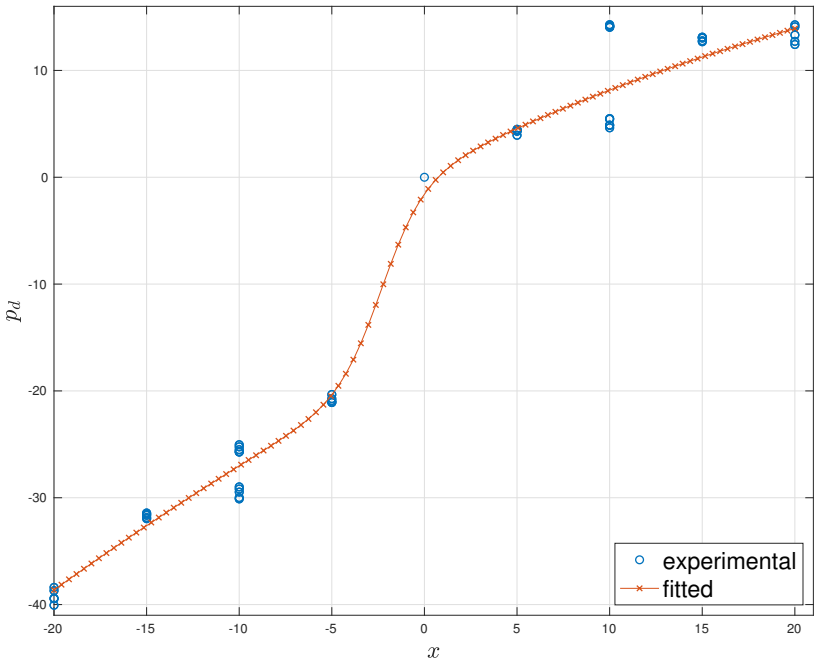


**FIGURE 23** The experimental and approximated $p_d = G(x)$ for the mem-dashpot component of all experiments in Group 1 in Table 2 using a FFNN with three hidden nodes

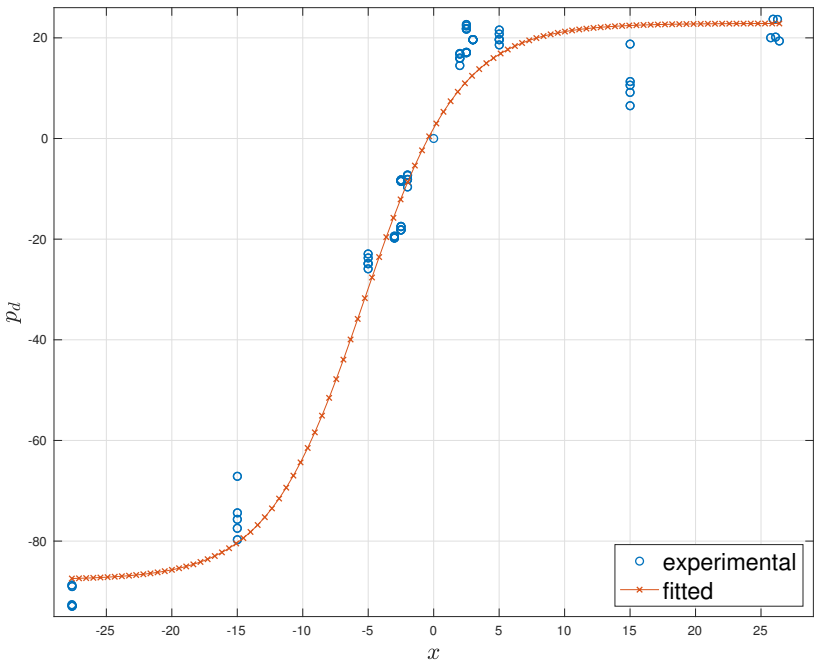


**FIGURE 24** The experimental and approximated $p_d = G(x)$ for the mem-dashpot component of all experiments in Group 2 in Table 2 using a FFNN with three hidden nodes

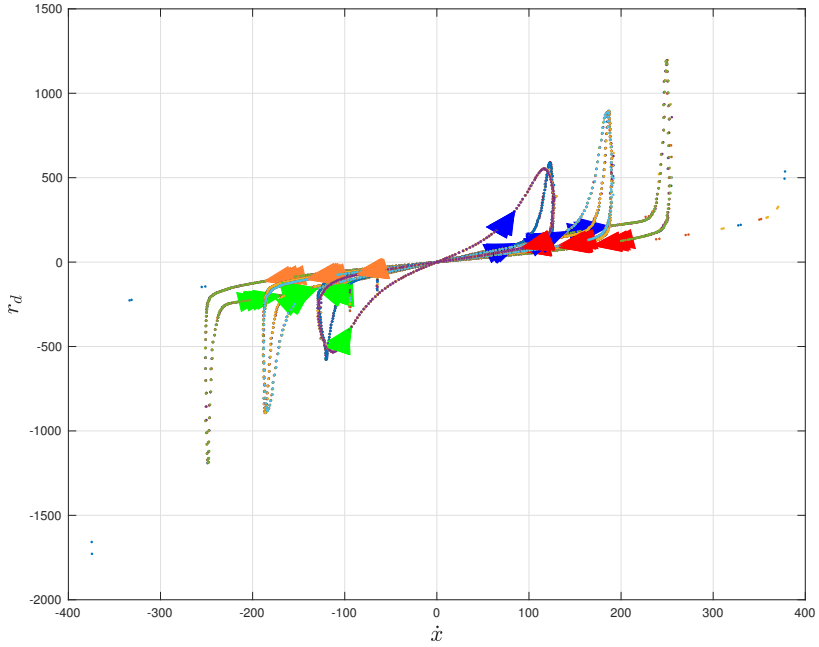


**FIGURE 25** The approximated $r_d = D(x)\dot{x}$ for the mem-dashpot component of all experiments in Group 1 in Table 2 using a FFNN with three hidden nodes

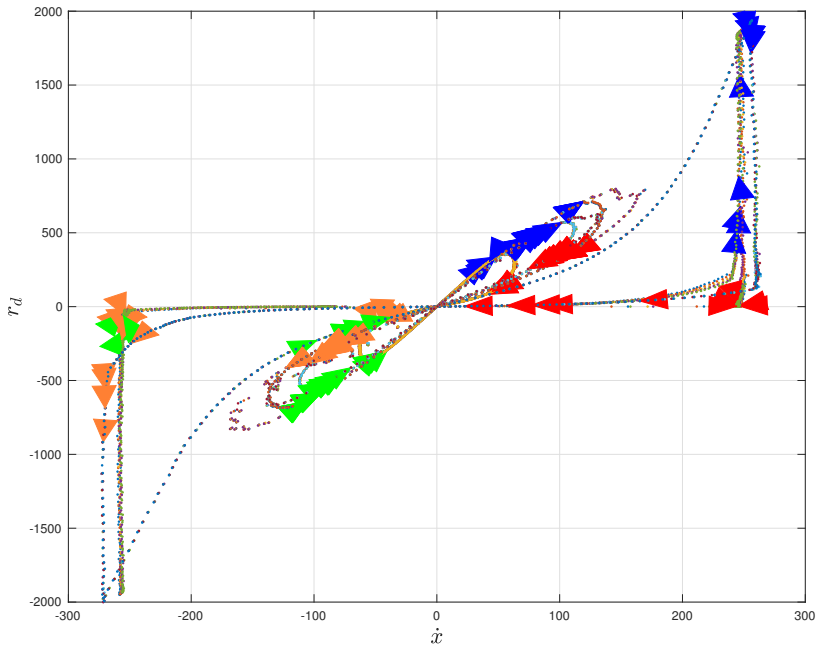


**FIGURE 26** The approximated $r_d = D(x)\dot{x}$ for the mem-dashpot component of all experiments in Group 2 in Table 2 using a FFNN with three hidden nodes

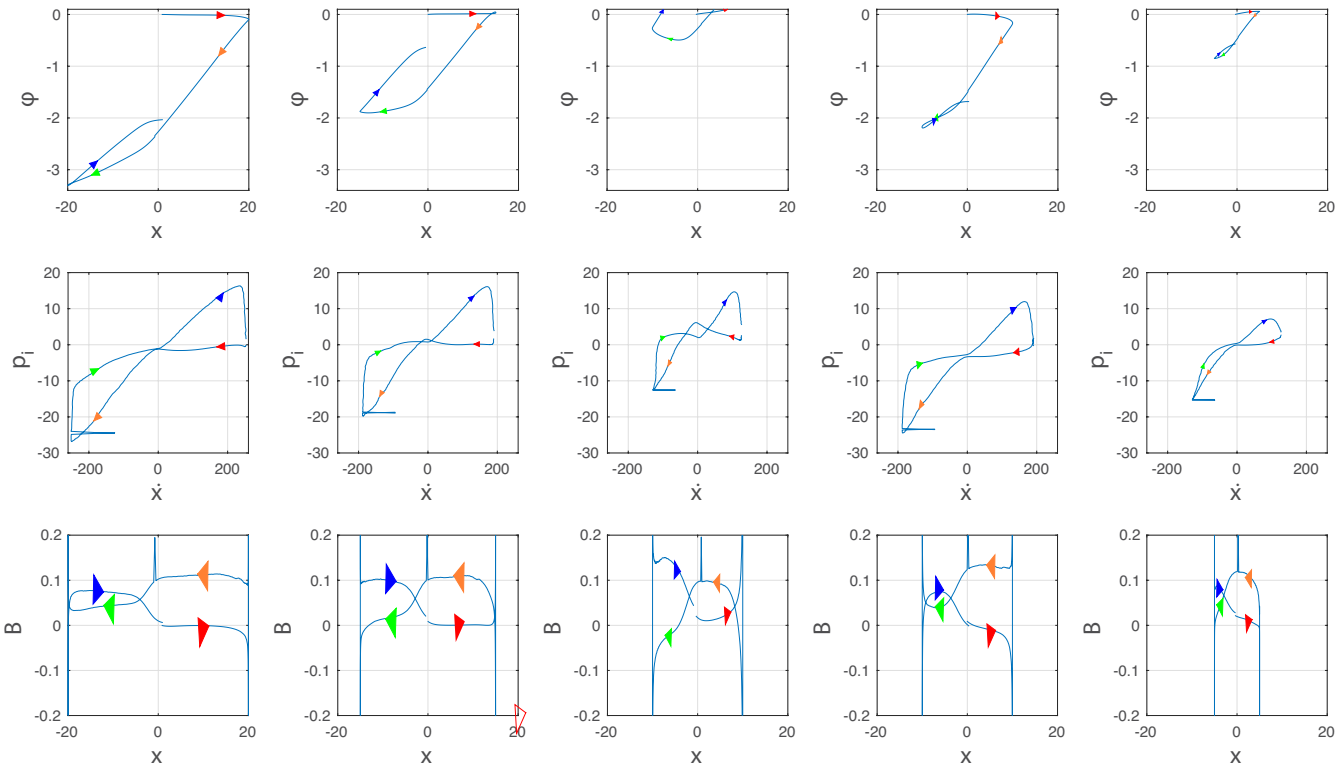


**FIGURE 27** The approximated $p_i = B(x)\dot{x}$ for the mem-inerter component for a typical one cycle: Group 1 in Table 2. From left to right, they are: 20mm 2Hz, 15mm 2Hz, 10mm 2Hz, 10mm 3Hz, and 5mm 4Hz. Notice: There are physically meaningless portions

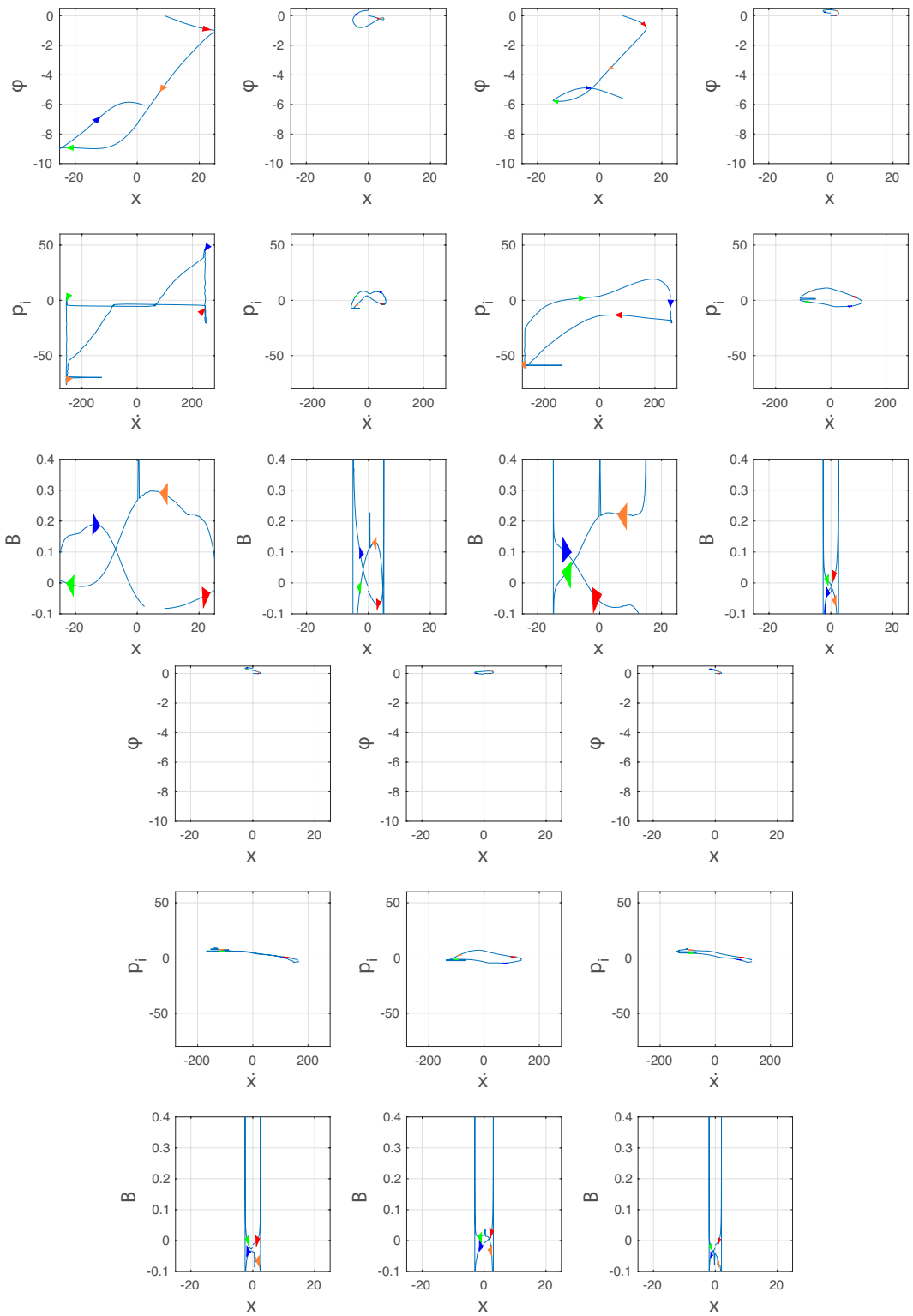


**FIGURE 28** The approximated $p_i = B(x)\dot{x}$ for the mem-inerter component for a typical one cycle: Group 2 in Table 2. From top to bottom and left to right, they are: 30mm 2Hz, 5mm 2Hz, 15mm 3Hz, 2.5mm 7Hz, 2.5mm 10Hz, 3mm 7Hz, and 2mm 10Hz. Notice: There are physically meaningless portions

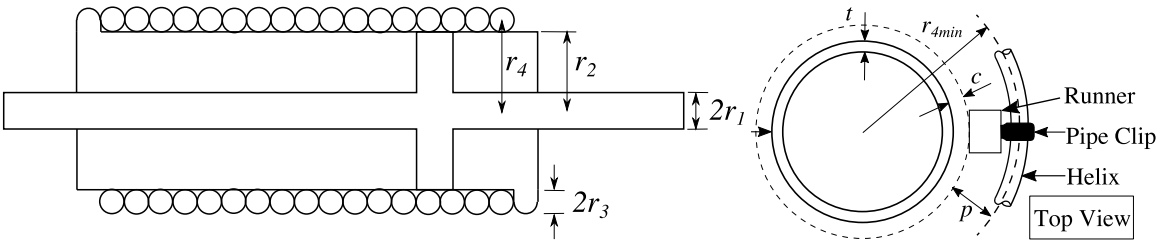


**FIGURE A1** Schematic diagram of the inerter design showing the longitudinal cross section, and the top view of the system

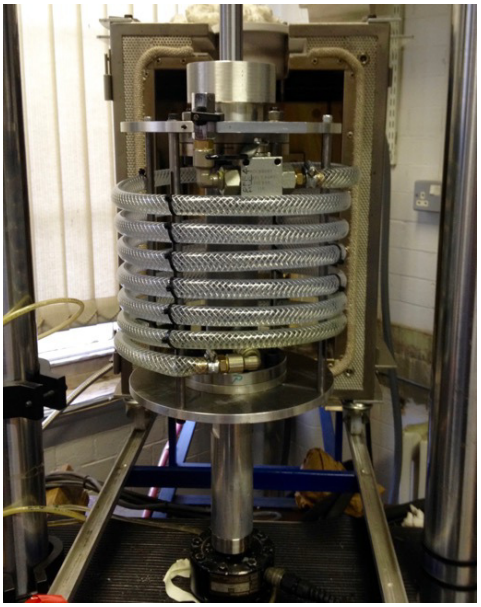

**FIGURE A2** Photograph of the inerter mounted vertically in the test machine showing the external helix piping